

## **Targeting IGF perturbs global replication through ribonucleotide reductase dysfunction**

Guillaume Rieunier<sup>1</sup>, Xiaoning Wu<sup>1</sup>, Letitia E. Harris<sup>2</sup>, Jack V. Mills<sup>1</sup>, Ashwin Nandakumar<sup>1</sup>, Laura Colling<sup>3</sup>, Elena Seraia<sup>4</sup>, Stephanie B. Hatch<sup>4</sup>, Daniel V. Ebner<sup>4</sup>, Lisa K. Folkes<sup>2</sup>, Ulrike Weyer-Czernilofsky<sup>5</sup>, Thomas Bogenrieder<sup>6, 7</sup>, Anderson J. Ryan<sup>2</sup>, Valentine M. Macaulay<sup>1,8</sup>

<sup>1</sup>Department of Oncology, University of Oxford, Old Road Campus Research Building, Oxford OX3 7DQ, UK

<sup>2</sup>CRUK/MRC Oxford Institute for Radiation Oncology, University of Oxford, Old Road Campus Research Building, Oxford, OX3 7DQ, UK

<sup>3</sup>Department of Oncology, Weatherall Institute of Molecular Medicine, Oxford, OX3 9DS, UK

<sup>4</sup>Target Discovery Institute, University of Oxford, Oxford OX3 7FZ UK

<sup>5</sup>Boehringer Ingelheim RCV GmbH & Co KG, Dr.-Boehringer-Gasse 5-11, 1121 Vienna, Austria

<sup>6</sup>AMAL Therapeutics, c/o Fondation pour Recherches Médicales, 1205 Geneva, Switzerland

<sup>7</sup>Department of Urology, University Hospital Grosshadern, Ludwig-Maximilians-University, Marchioninistrasse 15, 81377 Munich, Germany

<sup>8</sup>Oxford Cancer and Haematology Centre, Oxford University Hospitals NHS Foundation Trust, Churchill Hospital, Oxford OX3 7LJ UK

Corresponding author: Dr V. M. Macaulay, Department of Oncology, Old Road Campus Research Building, Roosevelt Drive, Oxford OX3 7DQ UK. Email: [valentine.macaulay@oncology.ox.ac.uk](mailto:valentine.macaulay@oncology.ox.ac.uk). Phone: +44(0)1865 617337.

**Running title:** IGFs regulate RRM2 and replication fork progression

**Keywords:** IGF-1R, replication stress, RRM2, ATM, synthetic lethality

**Conflict of interests:** VMM is a consultancy board member for Boehringer Ingelheim. TB is an employee and UWC a previous employee of Boehringer Ingelheim RCV.

**Word count:** The manuscript has an abstract of 232 words, Statement of significance 27 words, word count (main text: Introduction, Methods, Results, Discussion) of 4997, 50 references, 7 data figures, a Graphical abstract and a Supplementary Data file containing Methods, 2 Tables and 6 Figures.

## **Abstract**

Inhibition of IGF receptor (IGF-1R) delays repair of radiation-induced DNA double-strand breaks (DSB), prompting us to investigate whether IGF-1R influences endogenous DNA damage. Here we demonstrate that IGF-1R inhibition generates endogenous DNA lesions protected by 53BP1 bodies, indicating under-replicated DNA. In cancer cells, inhibition or depletion of IGF-1R delayed replication fork progression accompanied by activation of ATR-Chk1 signaling and the intra-S-phase checkpoint. This phenotype reflected unanticipated regulation of global replication by IGF-1 mediated via AKT, MEK/ERK, and JUN to influence expression of ribonucleotide reductase (RNR) subunit RRM2. Consequently, inhibition or depletion of IGF-1R downregulated RRM2, compromising RNR function and perturbing dNTP supply. The resulting delay in fork progression and hallmarks of replication stress were rescued by RRM2 overexpression, confirming RRM2 as the critical factor through which IGF-1 regulates replication. Suspecting existence of a backup pathway protecting from toxic sequelae of replication stress, targeted compound screens in breast cancer cells identified synergy between IGF inhibition and ATM loss. Reciprocal screens of ATM-proficient/deficient fibroblasts identified an IGF-1R inhibitor as the top hit. IGF inhibition selectively compromised growth of ATM null cells and spheroids and caused regression of ATM null xenografts. This synthetic lethal effect reflected conversion of single-stranded lesions in IGF-inhibited cells into toxic DSBs upon ATM inhibition. Overall, these data implicate IGF-1R in alleviating replication stress, and the reciprocal IGF:ATM co-dependence we identify provides an approach to exploit this effect in ATM-deficient cancers.

## **Statement of Significance**

This study identifies regulation of ribonucleotide reductase function and dNTP supply by IGFs and demonstrates that IGF axis blockade induces replication stress and reciprocal co-dependence on ATM.

## Introduction

Type 1 insulin-like growth factor receptor (IGF-1R) is a receptor tyrosine kinase (RTK) expressed by most common cancers, and promotes proliferation, cell survival and invasion. These effects are mediated via multiple signalling pathways including phosphatidylinositol 3-kinase–AKT–mammalian target of rapamycin (PI3K-AKT-mTOR) and mitogen-activated protein kinase kinase–extracellular signal-regulated kinases (MEK-ERK) (1). IGF-1R is required for cellular transformation by oncogenes including SV40 and RAS, and can itself induce transformation when overexpressed (2). We and others found that IGF-1R overexpression associates with clinical radioresistance in breast and prostate cancer (3, 4), with evidence that IGF-1R targeting sensitizes to DNA damaging cytotoxic drugs and ionizing radiation (IR) *in vitro* and *in vivo* (5-7). We further reported that IGF-1R inhibition delays repair of IR-induced DNA double strand breaks (DSBs) and inhibits homologous recombination (HR) and non-homologous end-joining (NHEJ) in repair reporter assays (7). The ability of IGF-1R to regulate repair of exogenous DNA damage appears independent of its well-characterized ability to protect from apoptosis (7), and may require IGF-regulated interaction between the docking protein insulin receptor substrate-1 (IRS-1) and RAD51 (8), and IGF-induced activation of PI3K-AKT-mTOR and MEK-ERK pathways, both reported to mediate radioresistance (9, 10).

While this evidence supports a role for the IGF axis in the response to IR-induced DNA damage, IGFs have not previously been implicated in maintaining replication integrity in the absence of exogenous damage. We previously reported that IGF-1R inhibited or depleted tumor cells accumulate  $\gamma$ H2AX foci, representing initial evidence of endogenous DNA lesions (11), but their origin was unknown. Foci formed by  $\gamma$ H2AX indicates H2AX phosphorylation at damage sites by PI3K-like kinases ataxia telangiectasia mutated (ATM), ataxia telangiectasia and Rad3-related protein (ATR), and DNA-dependent protein kinase (12). ATM is activated by diverse DNA structures in addition to IR-induced DSBs, while ATR responds to extended single-stranded DNA (ssDNA).

Here, we identify the source and functional consequences of endogenous DNA lesions in cells where IGF signalling is suppressed. We discover unanticipated regulation by IGF-1R of ribonucleotide reductase (RNR) function and dNTP supply; as a consequence, IGF axis blockade compromises completion of global DNA replication, delaying replication fork progression and allowing under-replicated DNA to progress through mitosis. We also reveal that replication stress in IGF-inhibited cells is maintained at a tolerable level by ATM, preventing conversion of single strand breaks (SSBs) into DSBs. Thus, replication stress in IGF-inhibited cells associates with a state of reciprocal co-dependence on ATM that can be exploited in therapy.

## Methods

**Cell lines.** Breast cancer cell lines HCC1143, MCF7, T47D and ZR-75-1 were obtained in 2015 from Anthony Kong (Institute of Cancer and Genomic Sciences, University of Birmingham), HCT15 cells in 2018 from Walter Bodmer (Department of Oncology, University of Oxford), BXP-3 in January 2020 from Eric O’Neil (Department of Oncology, University of Oxford), *ATM* WT and *ATM* null H322 cells in 2019 from Sebastian Nijman, Nuffield Department of Medicine, University of Oxford and KPL1 (2016), LoVo, SK-CO-1, immortalized *ATM* WT MRC5-SV2 in 2018 from the European Collection of Authenticated Cell Cultures (ECACC) and *ATM*<sup>-/-</sup> AT5BIVA fibroblasts in 2018 from The Coriell Institute for Medical Research, MiaPaCa-2 in March 2020 from the American Type Culture Collection (ATCC), paired *ATM* proficient and deficient MiaPaCa-2 in March 2020 from Duncan Jodrell and Frances Richards, University of Cambridge. Cell cultures were cryopreserved at early passage and used within 20 passages. Cell lines were mycoplasma-free (MycoAlert, Lonza Rockland Inc.) and cell line identity was authenticated by STR genotyping (Eurofins Medigenomix Forensik GmbH).

**Gene knockdowns were performed** as described in (7, 13) using 2-3 separate siRNAs to deplete each target, including 3 IGF-1R siRNAs (siIGF-1R\_1, \_2, \_3; where no numbering is stated, siIGF-1R1 was used).

**Cell viability, doubling time, spheroid and cell death assays** were performed as described in Supplementary methods.

**Western blotting, immunofluorescence and flow cytometry** were performed as described (7, 13) using antibodies in Supplementary Table S1.

**DNA fiber assays** were performed as detailed in Supplementary Methods. Fork velocity was converted to kb/min based on tract length (μm) and duration of incubation with 5-chloro-2’deoxyuridine (CldU) and 5-iodo-2’deoxyuridine (IdU; 20min each).

**Nucleotide assay** was performed as described in Supplementary methods and (14).

**Reverse-transcription-quantitative PCR (qPCR)** was performed following extraction of RNAs and reverse-transcription using Pure Link RNA Mini RNA extraction kits (Ambion) and SuperScript III First-Strand Synthesis SuperMix (Invitrogen), amplifying cDNAs using primers listed in Supplementary Methods with Sybr Green PCR Mix (Applied Biosystems) on a 7500 Fast RT-PCR System (Applied Biosystems).

**Luciferase Assays:** MCF7 cells were transfected with pcDNA 3.1 (#V79520, Invitrogen) or pcDNA3.1 RRM2 (Addgene, Plasmid #13796) using Lipofectamine 3000<sup>TM</sup> (Invitrogen). On day 2 cells were siRNA-transfected, reseeded on day 3 into 96-well plates and on day 4 luciferase assays were performed (ONE-Glo<sup>TM</sup> EX Luciferase assay, Promega). Values were expressed as relative light units per µg protein.

**MCF7 stably-overexpressing RRM2:** MCF7 cells were transfected with pcDNA 3.1 (#V79520, Invitrogen) or pcDNA3.1 RRM2 (Addgene, Plasmid #13796) using Lipofectamine 3000 (#L3000001, Thermo Fisher Scientific). After selection with 800 µg/mL G418 (Sigma-Aldrich) for 30 days to obtain stable clones, RRM2 expression was tested by western blot.

**Compound screens:** Two screens were performed in duplicate as detailed in Supplementary methods. In brief, the first screen tested five ER+ breast cancer cell lines with a 60-compound custom library at 100 nM, 1 µM and 10 µM alone or with 1 µM xentuzumab. Screen replicate correlation was 0.97 and the screen Z-Factor calculated using the positive control for viability inhibition (PLK1 inhibitor BI-2536) was 0.64 at 100 nM, 0.68 at 1 µM and 0.72 at 10 µM, indicating high-quality screens. Secondly, ATM WT MRC5-SV2 and ATM-/- AT5BIVA fibroblasts were tested against a 188-compound kinase chemogenomic set. The screen Z-Factor calculated using the positive control for viability inhibition (camptothecin analogue SN-38) was 0.63 and 0.81 at 0.1 µM for ATM WT and mutated cells respectively, and 0.83 and 0.81 at 1 µM, indicating a high-quality screen.

**Single cell gel electrophoresis.** Alkaline and neutral comet assays were performed as described in Supplementary methods. Comets were visualised at 100× magnification using an epifluorescence

microscope (Ni-E, Nikon) and Komet v.5.5 software (Andor), analyzing 100 comets per condition and quantifying tail DNA as % total DNA.

***In vivo* experiments** were performed under UK Home Office approved Project Licence PPL 30/3395 and PIL I9BC08CD7. Before submitting to the UK Home Office, the Project Licence was reviewed and approved by the Oxford University Animal Welfare and Ethical Review Board (AWERB), in line with the Oxford University Policy on use of animals in research (<https://www.ox.ac.uk/news-and-events/animal-research/university-policy-on-the-use-of-animals-in-scientific-research>). Animals were treated and tissues processed for immunohistochemistry as described in Supplementary methods, using antibodies listed in Supplementary Table S1.

**Statistics.** GraphPad Prism v7 was used to perform Student's t-test to compare means of 2 groups, one-way ANOVA to compare >2 groups, two-way ANOVA to compare 2 variables,  $\geq 2$  groups. All tests were 2-sided and  $p < 0.05$  (\*),  $p < 0.01$  (\*\*) and  $p < 0.001$  (\*\*\*) were considered significant.



## Results

### IGF axis inhibition induces endogenous DNA damage and replication stress

To explore the role of IGF-1R in protection from endogenous DNA damage we used *IGF1R* gene silencing and IGF neutralizing antibody xentuzumab (15). Initially, we detected increased  $\gamma$ H2AX foci in xentuzumab-treated MCF7 breast cancer cells, at xentuzumab concentrations that inhibited IGF-1R and AKT-S6 phosphorylation (Figure 1A-B). ERKs were not inhibited in MCF7 although were suppressed in other breast cancer cell lines (Supplementary Figure S1A). Xentuzumab also caused concentration-dependent increase in lesions marked by 53BP1 (Figure 1C), and cyclin A-53BP1 co-staining indicated that both xentuzumab and IGF-1R depletion increased 53BP1 signal in G1 (cyclin A-negative) cells (Figure 1D). These findings suggest appearance in G1 of 53BP1 nuclear bodies. These lesions form to protect incompletely-replicated DNA from erosion during mitosis (16), and their presence suggests a state of replication stress (17). This finding prompted us to perform DNA fiber assays, revealing significantly shortened DNA tracts in IGF-1R-depleted MCF7 (Figure 1E-F) and KPL1 cells (Supplementary Figure S1B). Replication fork speed was also reduced by IGF-1R depletion (Figure 1G), with comparable reduction in tract length and fork speed within 6h exposure to xentuzumab (Figure 1H-I), suggesting a direct effect of IGF blockade. There was no increase in stalled or collapsed forks, identified as CldU (red) only signal or CldU tracts followed by short IdU (green) tracts (Supplementary Fig S1C). We also measured sister fork tracts, which extend in opposite directions from a unique replication origin. Sister forks progress at similar rates under physiological conditions or during replication stress not due to a physical impediment, and at different rates if one fork encounters obstructing DNA lesions (17, 18). We found no significant sister fork asymmetry upon IGF-1R depletion (Figure 1J), suggesting that replication stress originated from global reduction in replication. Supporting the presence of unreplicated single-stranded DNA (ssDNA), we detected increased S33 phosphorylation of replication protein A (RPA32) in IGF-1R depleted cells (Supplementary Figure S1D).

If DNA replication was indeed incomplete, ssDNA regions should trigger activation of the checkpoint kinase ATR (19). Therefore, we assessed S345-CHK1 phosphorylation, a marker of ATR activation at the replication fork, finding enhanced CHK1 phosphorylation in IGF-1R-depleted and xentuzumab-treated MCF7 and KPL1 cells (Figure 2A, Supplementary Figure S1E-F). ATR activation should inhibit origin firing (12), and indeed newly-fired origins were reduced after IGF-1R depletion (Figure 2B). IGF-1R depletion also induced accumulation of cells in S-phase, detectable in asynchronous cultures (Supplementary Figure S2A). We also depleted IGF-1R in the context of cell cycle synchronization using nocodazole, which had the predicted effect of G2-M arrest (Supplementary Figure S2B). In cells transfected with control or IGF-1R siRNA prior to nocodazole treatment, there was significant S-phase accumulation (Figure 2C-D) associated with reduction in the G2-M population (Supplementary Figure S2B) representing further evidence of activation of ATR and the intra-S checkpoint. IGFs are well-known to promote G1/S and G2/M checkpoint progression via cyclin upregulation, CDK activation and Rb phosphorylation (1). Our data show that by regulating fork progression, IGFs also influence the rate of transition through S-phase, and reveal hallmarks of replication stress when IGF-1R is non-functional.

### **IGF-1 regulates RRM2 expression and RNR activity**

Having identified replication fork delay and shortened but symmetrical sister forks in IGF-1R depleted cells (Figure 1E-F, J), we hypothesized that IGFs regulate the supply of substrates for replication. Quantification of deoxyribonucleoside triphosphates (dNTPs) revealed significant reduction in dATP content in IGF-1R-depleted MCF7 cells, while dTTP and dGTP were unchanged and dCTP undetectable (Figure 3A; Supplementary Figure S3A-B). In HCT15 colorectal cancer (CRC) cells, which proliferate more rapidly than MCF7, dATP content was reduced by IGF-1R depletion as in MCF7, while dCTP, dGTP and dTTP were unaltered (Figure 3B). These differential changes led us to investigate RNR, which converts ribonucleotide diphosphates to deoxyribonucleotides, the rate-limiting step for dNTP production (20). We noted that a microarray study in MCF7 cells had

generated an IGF gene signature that associates with adverse outcome in breast cancer, and included upregulation of cyclins, components of the replication machinery and the regulatory subunit M2 (RRM2) of RNR (21). In the same cell line, we found that RRM2 mRNA and protein were upregulated by IGF-1 and downregulated by xentuzumab and IGF-1R depletion (Figure 3C-F). Although IGF axis blockade induced significant RRM2 downregulation, we speculate that residual RRM2 protein accounts for lack of effect on dCTP, dGTP and dTTP (Figure 3A-B). IGF-1R depletion did not affect catalytic subunit RRM1 or alternative regulatory subunit p53R2 (Figure 3E, Supplementary Figure S3C-D). RRM2 was also downregulated in IGF-1R depleted KPL1, HCC1143, ZR-75-1 and T47D breast cancer, DU145 prostate cancer and U2OS osteosarcoma cells (Figure 3G, Supplementary Figure S3E). The magnitude of RRM2 downregulation induced by IGF-1R depletion (60-80% of levels in control-transfectants) appeared unrelated to cell line proliferation rate, quantified as doubling time (Supplementary Figure S3E right panel).

To investigate regulators of RRM2 expression we assessed the principal IGF-1R effectors MEK-ERK and AKT. After 3-24 hr, IGF-induced ERK activation was clearly detectable in MCF7 cells (Figure 3H), in contrast to the absent ERK response in Figure 1B, perhaps reflecting the shorter IGF stimulation (15 min) used in Figure 1B to test effects of xentuzumab on IGF-1R phosphorylation, which is likely to be transient. MEK inhibitor trametinib and AKT inhibitor AZD5363 were confirmed to inhibit ERK and S6 phosphorylation respectively, and both agents suppressed IGF-induced RRM2 upregulation (Figure 3H-I). We recently reported that IGF-1R is recruited to proximal promoters to influence gene transcription (13), but our ChIP-seq did not detect IGF-1R at the *RRM2* promoter (Supplementary Figure S3F), suggesting that IGFs regulate RRM2 via canonical signalling, not via non-canonical nuclear translocation. The RRM2 promoter contains motifs for multiple transcription factors ([www.genecards.org/cgi-bin/carddisp.pl?gene=RRM2](http://www.genecards.org/cgi-bin/carddisp.pl?gene=RRM2)), including E2F1 and FOS/JUN dimer AP-1, and we investigated the contribution of these candidate RRM2 regulators. E2F1 depletion downregulated RRM2, and IGF-1R:E2F1 co-depletion achieved more profound RRM2 downregulation than was achieved by depleting either factor alone (Supplementary Figure S3G)

suggesting that IGF-1R regulates RRM2 via different pathway(s) from E2F1. JUN depletion induced minor RRM2 downregulation (to 67-72% of control levels), and IGF-1R:JUN co-depletion achieved no greater RRM2 downregulation than depletion of IGF-1R or JUN separately (Figure 3J). This preliminary result suggested JUN as a mediator of IGF effects on RRM2. To quantify the role of JUN we transfected MCF7 cells with *RRM2* luciferase promoter reporter, finding that promoter activity was reduced by IGF-1R or JUN depletion, and was not further reduced by depleting both factors (Figure 3K). These analyses suggest an epistatic relationship between IGF-1R and JUN, consistent with the function of JUN as a transcriptional effector of MEK-ERK (22), and support a model in which IGFs regulate RRM2 expression at least in part via MEK-ERK-JUN.

We used two models to investigate the role of RRM2 in the replication stress phenotype induced by IGF-1R depletion. First, we utilized RRM2 stably-overexpressing U2OS cells (23), confirming constitutive RRM2 overexpression that was resistant to IGF-1R knockdown (Figure 4A). In control (empty vector) transfectants, xentuzumab induced phosphorylation of ATR targets CHK1 and RPA, consistent with results in MCF7 (Supplementary Figure S1D-F), while RRM2 overexpression suppressed CHK1 and RPA phosphorylation (Figure 4B). We quantified 53BP1 bodies as surrogate markers of under-replicated DNA, finding increased 53BP1 bodies in IGF-1R depleted U2OS control cells, also consistent with MCF7 (Figure 1D), and this was completely prevented by RRM2-overexpression (Figure 4C). We generated a second model, stably-transfecting MCF7 cells with control vector or RRM2 cDNA, and used these cells to perform DNA fiber assays, cell cycle analysis and 53BP1 immunofluorescence. In control transfectants, IGF-1R depletion caused significant shortening of DNA tracts and modest but significant S-phase accumulation (Figure 4D-E, Supplementary Figure S3H) comparable to effects in parental MCF7 (Figure 1E-F, Figure 2C-D). In MCF7 cells stably overexpressing RRM2 there was partial rescue from DNA tract shortening after IGF-1R depletion (Figure 4D-E) and no increased in S phase cells (Supplementary Figure S3H). Consistent with data in the U2OS model (Figure 4C), RRM2 overexpression also rescued MCF7 cells from xentuzumab-induced increase in 53BP1 bodies, partial rescue likely attributable to reduction in

endogenous RRM2 upon IGF-1R depletion (Figure 4F-G). We also tested RNR inhibitor didox, finding no greater viability suppression in MCF7 cells treated with didox plus xentuzumab compared with didox alone (Supplementary Figure S3I). These data identify RRM2 as a central factor in the replication stress phenotype induced by IGF-1R depletion.

### **ATM loss is synthetically lethal to IGF-inhibited cells and tumors**

Given that IGF axis targeting significantly perturbed replication fork progression, we quantified effects on proliferation, tested xentuzumab in the five luminal breast cancer cell lines in which IGF-1R depletion downregulated RRM2 (Figure 3G). Using xentuzumab at 1  $\mu$ M, approximating to the steady-state plasma concentration at the dose chosen for Phase II evaluation (24), xentuzumab caused relatively little inhibition of cell viability (Figure 5A). This minor effect in the face of significant replication stress suggested a backup pathway that alleviates toxic effects of replication intermediates, allowing a threshold of tolerable replication stress. To identify components of such a pathway, we performed a targeted compound screen using kinase, cell cycle, DNA replication and repair inhibitors in the five ER+ breast cancer cell lines. We discuss MCF7 data here, and will report other outcomes separately. Assessment of the 12 top-ranked compounds achieving greatest viability inhibition with xentuzumab revealed partial overlap at the three screened compound concentrations (Figure 5B). Included here were inhibitors of PARP, EGFR and MEK (Supplementary Table S2), already identified as showing potential for combination with IGF-1R blockade (1). Of five compounds ranked highly at all concentrations (Supplementary Figure S4A), only one, ATM inhibitor KU-55933, had not previously been identified as an attractive partner for IGF co-inhibition. We validated KU-55933 as a screen hit in MCF7 and ZR-75-1 cells, finding that KU-55933 had little effect in control-treated cells, consistent with the known lack of toxicity of ATM inhibition in the absence of exogenous DNA damage (25), while addition of xentuzumab significantly inhibited viability at KU-55933 concentrations  $\geq 300$  nM (Figure 5C; Supplementary Figure S4B). We confirmed that at these concentrations, KU-55933 inhibited irradiation-induced phosphorylation of ATM target KAP1, both in

the absence and presence of xentuzumab (Figure 5C-D; Supplementary Figure S4C). Xentuzumab also caused synergistic inhibition of the viability of MCF7, MiaPaca-2 and BXPc-3 cells when combined with a second ATM inhibitor, AZD0156 (Figure 5E, Supplementary Figure S4D-E) at clinically-achieved sub-micromolar concentrations (25). Furthermore, MCF7 cell death was significantly increased in cells exposed to xentuzumab with KU-55933 or AZD0156 (Figure 5F-G, Supplementary Figure S5A). Given evidence of ATR activation upon IGF-1R targeting (Figure 3A, Supplementary Figure S1D-F), we tested for synthetic lethality with ATR inhibitors AZ20 or VE-821, finding no increased toxicity on addition of xentuzumab (Supplementary Figure S5B-C). These results support ATM-specific effects of the combination with KU-55933 or AZD0156.

ATM mutations and deletions are detectable in a significant proportion of epithelial cancers including CRC (12%), lung (10%), prostate (7%), pancreatic (4%) and breast (3.5%) cancers (cbioportal.org). ATM protein loss is reported in  $\leq 60\%$  of sporadic breast cancers and  $\sim 13\%$  of pancreatic ductal adenocarcinomas (PDAC) (26, 27), significantly exceeding ATM mutation rates, reflecting complex regulation of ATM expression. Given this evidence of frequent ATM loss, we took five approaches to test IGF dependence in ATM deficient cells. First, we accessed publicly-available data from 926 cancer cell lines (cancerrxgene.org, kobic.kr), including cell lines harboring homozygous ATM mutations, which lack functional ATM. Homozygous  $ATM^{-/-}$  cell lines were more sensitive to IGF-1R inhibitor BMS-754807 ( $p=0.0018$ ), with a trend to increased sensitivity to linsitinib ( $p=0.08$ , Figure 6A, Supplementary Figure S6A). Secondly, we took an unbiased approach to assess IGF-1R function in  $ATM^{+/+}$  and null (A-T) fibroblasts, confirming ATM status and using these cells in a kinase inhibitor screen (Figure 6B, Supplementary Figure S6B). Consistent with identification of ATM as a hit in the xentuzumab screen (Figure 5B-C), IGF-1R inhibitor GSK1838705 was the top synthetic lethal interaction in  $ATM^{-/-}$  fibroblasts when testing compounds at 1  $\mu$ M, and the second-ranked hit at 0.1  $\mu$ M (Supplementary Figure S6C). Low-throughput assays confirmed that  $ATM^{-/-}$  fibroblasts were significantly more sensitive to IGF-1R kinase inhibitor BI-885578 (28) and xentuzumab (Figure 5C; Supplementary Figure S6D). BI-885578 suppressed IGF-induced AKT

activation in both ATM proficient and deficient cells (Figure 6C, right panel), excluding failure of target inhibition as causing resistance of *ATM*<sup>+/+</sup> cells to IGF-1R blockade. Thirdly, in an isogenic ATM proficient/deficient H322 lung cancer model (29), we found that *ATM*-null cells were significantly more sensitive to BI-885578 (Supplementary Figure S6E). H322 cells are non-tumorigenic (29), so as a fourth approach we sought alternative *ATM*-null models for *in vivo* testing. CRC cell lines LoVo and SK-CO-1 both harbor WT *PTEN* and  $\beta$ -catenin and mutant *KRAS* and *APC* (28) but differ in ATM status, SK-CO-1 being ATM null (30). LoVo cells were resistant to IGF-1R inhibition, consistent with (28), despite effective suppression of IGF-induced AKT phosphorylation, while SK-CO-1 cells were significantly more sensitive to xentuzumab and BI-885578 (Figure 6D, (Supplementary Figure S6F).

We next asked whether ATM status influences response to IGF-1R inhibition in 3D models. Firstly, we treated mice bearing SK-CO-1 xenografts with xentuzumab, dose and schedule as (15). Xentuzumab was well-tolerated (Supplementary Figure S6G), significantly inhibited growth of ATM-null SK-CO-1 tumors (Figure 6E-F, Supplementary Figure S6H) and suppressed phospho-Ser473 AKT in both human tumor and mouse skin (Figure 6G), as expected given cross-reactivity with murine IGFs (15). Cleaved caspase 3 signal was increased in xentuzumab-treated tumors, with no evidence of apoptosis in normal mouse skin (Figure 6G). RRM2 expression is known to increase during S phase (20), likely explaining high expression in hair follicles, and was significantly downregulated in xentuzumab-treated tumors particularly when considering moderate-strong (2-3+) signal (Figure 6G, Supplementary Figure S6I). We assessed BrdU incorporation to measure DNA replication *in vivo*, finding heterogeneous incorporation with strong signal in tumor cells and hair follicles (Figure 6G, Supplementary Figure S6J), and significant reduction in moderate-strong BrdU signal after xentuzumab treatment, consistent with replication defects induced by IGF-1R targeting *in vitro* (Figure 1E-G). Finally, we obtained isogenic human MiaPaCa2 pancreatic cancer cell lines that are ATM proficient or rendered ATM null by genome editing (31). We confirmed their ATM status (Supplementary Figure S6K), and used 3D spheroids to assess anchorage-independent growth. ATM-deficient spheroids were highly sensitive to xentuzumab, while ATM-proficient spheroids were

significantly growth inhibited by xentuzumab plus ATM inhibitor AZD0165 but not by either drug alone (Figure 6H-I).

### **Loss of functional ATM converts replication stress-associated SSBs in IGF inhibited cells into DSBs**

Next, we explored the role of ATM in alleviating toxic effects of replication stress in IGF inhibited cells. We had speculated that ATM undergoes protective activation in response to DNA lesions induced by IGF-inhibition. However, we earlier found no evidence that xentuzumab induced KAP1 phosphorylation, indicating that ATM was not activated (Figure 5D; Supplementary Figure S4C). Similarly, there was no evidence from KAP1 or ATM phosphorylation that ATM was activated by IGF-1R depletion (Supplementary Figure S6L). As a first approach to assessing the contribution of ATM in protecting replication forks, we performed DNA fiber assays on LoVo and SK-CO-1 cells, matched for major mutations and differing in ATM status. Upon IGF-1R depletion we observed significant shortening of DNA tracts in SK-CO-1 cells ( $16.1 \pm 4\mu\text{m}$  to  $8.7 \pm 3.7\mu\text{m}$ ; Figure 7A), consistent with effects in MCF7 and KPL1 cells (Figure 1E-F; Supplementary Figure S1B). The basal rate of fork progression was slower in LoVo, and there was only a small change upon IGF-1R depletion ( $10 \pm 2.9\mu\text{m}$  to  $9 \pm 2.6\mu\text{m}$ ; Figure 7A), suggesting a protective role for ATM. Secondly, we analysed 53BP1 bodies, finding, as previously (Figure 1D), that 53BP1 bodies were increased in xentuzumab-treated G1 (cyclin A-negative) cells. However, no 53BP1 bodies were detected after treatment with AZD0156 alone or with xentuzumab (Figure 7B), consistent with the importance of ATM in phosphorylating the 53BP1 SQ/TQ cluster required for 53BP1 oligomerization into 53BP1 bodies (16). The absence of 53BP1 bodies after dual ATM:IGF inhibition suggests inadequate protection of under-replicated DNA in replication-stressed IGF-inhibited cells.

Finally, we investigated the nature of the DNA damage induced by IGF-inhibition in the presence and absence of functional ATM, hypothesizing that ATM prevents conversion of tolerable DNA lesions to an intolerable form. If so, this could potentially explain relatively minor inhibitory effects of xentuzumab on viability (Figure 6A) despite significant induction of replication stress (Figure 1A-D).



MCF7 cells were treated with xentuzumab, KU-55933 or the combination, quantifying SSBs and DSBs by alkaline comet assay, and DSBs only by neutral comet assay. Xentuzumab induced DNA fragmentation in alkaline but not neutral assays (Figure 7C-D), suggesting that the damage was predominantly SSBs, comparable to effects of RNR inhibitor hydroxyurea (32). The xentuzumab:KU-55933 combination significantly increased DNA fragmentation, exceeding the cumulative effects of each drug separately, in both alkaline and neutral assays (Figure 7C-D), suggesting appearance of DSBs, potentially originating from SSBs that accumulate after IGF-1R inhibition. Unrepaired DSBs are highly toxic (12, 33), accounting for the significant increase in cell death in cells exposed to xentuzumab with KU-55933 or AZD0156 (Figure 5F-G).

## Discussion

RRM2 is the regulatory subunit of RNR, the sole enzyme capable of de novo dNTP synthesis (20). RRM2 is frequently overexpressed in cancers and associates with adverse outcomes (34). Therefore, it is of therapeutic relevance that its expression is regulated by a druggable target, IGF-1R. RRM2 expression is already known to be coordinated at the transcriptional, translational and post-translational levels by BRCA1, CDK4/6, mTORC1, WEE1/SETD2 and SCF<sup>Cyclin F</sup>/CDKs respectively (23, 35-37). Here, we identify IGF-1R as causing potent RRM2 upregulation, with comparable effects at the level of mRNA, protein and promoter activity, supporting transcriptional rather than post-transcriptional/translational regulation. Our data also implicate AKT, MEK-ERK and JUN in mediating RRM2 expression. RRM2 downregulation by AKT inhibition is consistent with a role for mTORC1, although both RRM1 and RRM2 were downregulated by mTORC inhibition (36) unlike the RRM2-specific effect we observed. MEK-ERK involvement is implicated by reports of RRM2 upregulation in KRAS-driven CRC and PDAC cells (although the mechanism was not explored), and by downregulation of DDR proteins including RRM2 following MEK-ERK inhibition in KRAS-mutant PDAC (10, 38).

IGFs are well-known to promote cell cycle progression, attributed previously to regulation of G1-S and G2-M checkpoints (1). We show that by regulating RRM2 and replication fork progression, IGFs also influence passage through S-phase. Thus, IGF axis blockade leads to RRM2 downregulation, shortened DNA tracts, RPA and CHK1 phosphorylation and intra-S checkpoint activation. These effects are induced by both pharmacological IGF axis inhibition and siRNA-mediated receptor depletion. We acknowledge that siRNA transfection could affect DNA integrity but consider that the comparable effects we report on RRM2 expression and fork dynamics support the IGF axis as a major regulator of RRM2 expression and DNA replication. There is a potential discrepancy in our finding of shortened replication tracts and reduced origin firing after IGF-1R depletion, since these changes should suppress BrdU incorporation and therefore reduce the S-phase fraction. In contrast, we

found an increase in IGF-1R depleted cells in S phase, accentuated by Nocodazole trap/release synchronization (Figure 3C-D). The reduced rate of replication we identify, shown by delayed incorporation of BrdU analogs IdU and CldU (Figure 1E-F), presumably results in delayed transit through S-phase. These findings suggest that the S-phase accumulation induced by IGF-1R depletion is explained by longer S-phase transit, resolving apparent discrepancy. IGFs have not previously been implicated in regulating fork progression in the absence of exogenous damage. However, replication fork delay induced by alkylating agent was reportedly exacerbated in IGF-1R null fibroblasts, implying that IGF-1R promotes DNA damage tolerance (39), and nuclear IGF-1R:PCNA interaction is reported to rescue forking stalling after HU treatment in HeLa cells (40). The implications for endogenous replication stress were not discussed in that report, but could relate to our finding that IGF-1 regulates RRM2 and dNTP supply.

The phenotype we identify upon IGF axis blockade represents the first example of replication stress induced by RTK inhibition, and contrasts with replication stress associated with positive oncogenic functions of MYC, CYCLIN E and RAS. Specific molecular mechanisms implicated here include increased origin firing and re-firing leading to re-replication, replication/transcription conflicts that generate R-loops, G-quadruplexes and other secondary structures, or through ROS generation or perturbation of dNTP metabolism (14, 41, 42), leading ultimately to exhaustion of replication substrates including dNTPs (33). This suggests that reduced supply of replication substrates represents a final common pathway leading to replication stress induced by both oncogene activation and IGF-blockade. Replication stress occurring during oncogene-induced senescence has been shown to be due to RRM2 downregulation (43), providing further parallels between molecular events triggered by oncogene activation and IGF inhibition.

Although IGF blockade induced marked replication stress with significant delay in replication fork progression, accumulation of ssDNA lesions and ATR-CHK1 activation, we found only minor reduction in cell viability in xentuzumab-treated breast cancer cells. This is reminiscent of minor cell

survival inhibition induced only by relatively high (~100 $\mu$ M) concentrations of hydroxyurea that targets dNTP synthesis by direct RNR inhibition (44). Given evidence of ATR activation in response to under-replicated DNA, we predicted that ATR activation was protective, and ATR inhibition would be toxic to IGF-inhibited cells. However, this was not so (Supplementary Figure S3F-G). Rather, the compound screens highlighted the toxicity of IGF:ATM co-inhibition, leading us to identify a role for ATM in protecting replication forks by preventing conversion of replication stress-associated DNA lesions into DSBs. ATM plays a pyramidal role in regulating the cellular response to DSBs, which can arise after mishandling of SSBs, in which case DSB repair via HR or NHEJ is critical because unrepaired DSBs lead to premature arrest of transcription and replication, chromosome breakage and cell death (12). Previous reports linking IGF signalling with ATM include the finding that ATM mutant fibroblasts downregulate IGF-1R (45), and our report of reduced ATM protein stability and kinase activity in IGF-1R-downregulated B16 melanoma cells (5), in retrospect likely reflecting apoptosis-mediated ATM protein cleavage (46). Recently, ATM mutation was identified as enhancing sensitivity to IGF-1R inhibition in bladder cancer cells (47); together with our data in breast cancer, CRC and PDAC models, this supports testing of ATM loss as a predictive biomarker for response to IGF axis inhibition.

Two novel roles have been described for ATM, distinct from its role in coordinating the DSB response, and which may be relevant here. First, ATM can be activated by unrepaired SSBs, triggering G1 arrest so that DNA repair can be completed; this avoids replicating damaged DNA which would result in DSB formation (48). Secondly, ATM is also reportedly activated by RRM2 knockdown, while loss of ATM function restores dNTP supply in RRM2-depleted cells via metabolic reprogramming to increase substrates for dNTP synthesis, suppressing hallmarks of replication stress and increasing proliferation (49). However, we found no evidence of ATM activation in the context of RRM2 downregulation and replication stress induced by IGF inhibition, although it is possible that SSBs were induced in IGF-inhibited cells below a threshold reportedly required to activate ATM (48). Furthermore, we found that loss of ATM function in the context of IGF-1R depletion or IGF inhibition

was not protective, but rather caused synergistic inhibition of cell viability and cell death. The mechanism(s) by which ATM protects from replication stress induced by IGF blockade are not the main focus here, but we speculate that synthetic lethality of IGF:ATM co-inhibition relates to failure to form protective 53BP1 bodies around incompletely-replicated DNA (Figure 7B) and/or a role in replication fork protection, consistent with more marked replication fork delay upon IGF-1R depletion in ATM-deficient CRC cells than cells expressing functional ATM (Figure 7A). Such a role has not previously been ascribed to ATM but there is precedent for repair proteins such as BRCA2 contributing to fork protection in the absence of activating phosphorylation (50), suggesting that ATM phosphorylation may not be a pre-requisite for a protective role in the context of replication stress.

In summary, we show here that IGF axis blockade downregulates RRM2 and delays replication fork progression, leading to accumulation of ssDNA lesions that are converted to DSBs by ATM co-inhibition. This transition from managed replication stress to DSB accumulation is new and has not been shown for inhibition of other RTKs. This newly-identified function of IGF-1R suggests that patients whose tumors lack ATM may be responsive to IGF blockade, and sheds new light on the regulation of global DNA replication.

## Acknowledgements

We acknowledge the assistance and expertise provided by Graham Brown from the Microscopy core facility, Department of Oncology, University of Oxford. We thank Hui Li from Huazhong University of Science and Technology, China for the generous gift of the pGL3-RRM2-firefly construct, Vincenzo D'Angiolella for the kind gift of U2OS cells over-expressing RRM2, Michael Sanderson (ex-Boehringer Ingelheim, now Merck) for the generous supply of BI 885578, Walter F. Bodmer and Jenny Wilding for the gift of HCT15 cells, Sebastian M.B. Nijman for H322 *ATM* CRISPR cells, Duncan Jodrell and Frances Richards for MiaPaCa2 WT and *ATM* CRISPR cells, Eric O'Neil for the gift of BXPC-3 and Walter F. Bodmer, Amato J. Giaccia and Tim Humphrey for comments on the manuscript. This study was supported by Breast Cancer Now (2014NovPR364), Cancer Research UK (C476/A27060), The Rosetrees Trust and John Black Charitable Foundation (M330-F1) and support to VMM from the NIHR Oxford Biomedical Research Centre and the Harrington Discovery Institute.

**Author contribution:** GR and VMM designed the study and GR performed most of the experiments, with additional data from XW, LH, AN, LC, ES, SH, DE and LKF. Xentuzumab was provided by UWC and TB, and AJR supervised the design and conduct of *in vivo* experiments. The manuscript was written by GR and VMM and reviewed by all co-authors.

## References

1. Simpson A, Petnga W, Macaulay VM, Weyer-Czernilofsky U, and Bogenrieder T, Insulin-Like Growth Factor (IGF) Pathway Targeting in Cancer: Role of the IGF Axis and Opportunities for Future Combination Studies. *Target Oncol.* **2017**;12:571-597.
2. Valentinis B and Baserga R, IGF-I receptor signalling in transformation and differentiation. *Mol Pathol.* **2001**;54:133-7.
3. Turner BC, Haffty BG, Narayanan L, Yuan J, Havre PA, Gumbs AA *et al.*, Insulin-like growth factor-I receptor overexpression mediates cellular radioresistance and local breast cancer recurrence after lumpectomy and radiation. *Cancer Res.* **1997**;57:3079-83.
4. Aleksic T, Verrill C, Bryant RJ, Han C, Worrall AR, Brureau L *et al.*, IGF-1R associates with adverse outcomes after radical radiotherapy for prostate cancer. *Br J Cancer.* **2017**;117:1600-1606.
5. Macaulay VM, Salisbury AJ, Bohula EA, Playford MP, Smorodinsky NI, and Shiloh Y, Downregulation of the type 1 insulin-like growth factor receptor in mouse melanoma cells is associated with enhanced radiosensitivity and impaired activation of Atm kinase. *Oncogene.* **2001**;20:4029-40.
6. Ferte C, Lorient Y, Clemenson C, Commo F, Gombos A, Bibault JE *et al.*, IGF-1R targeting increases the antitumor effects of DNA-damaging agents in SCLC model: an opportunity to increase the efficacy of standard therapy. *Mol Cancer Ther.* **2013**;12:1213-22.
7. Chitnis MM, Lodhia KA, Aleksic T, Gao S, Protheroe AS, and Macaulay VM, IGF-1R inhibition enhances radiosensitivity and delays double-strand break repair by both non-homologous end-joining and homologous recombination. *Oncogene.* **2014**;33:5262-73.
8. Trojanek J, Ho T, Del Valle L, Nowicki M, Wang JY, Lassak A *et al.*, Role of the insulin-like growth factor I/insulin receptor substrate 1 axis in Rad51 trafficking and DNA repair by homologous recombination. *Mol Cell Biol.* **2003**;23:7510-24.
9. Toulany M, Lee KJ, Fattah KR, Lin YF, Fehrenbacher B, Schaller M *et al.*, Akt promotes post-irradiation survival of human tumor cells through initiation, progression, and termination of DNA-PKcs-dependent DNA double-strand break repair. *Mol Cancer Res.* **2012**;10:945-57.
10. Estrada-Bernal A, Chatterjee M, Haque SJ, Yang L, Morgan MA, Kotian S *et al.*, MEK inhibitor GSK1120212-mediated radiosensitization of pancreatic cancer cells involves inhibition of DNA double-strand break repair pathways. *Cell Cycle.* **2015**;14:3713-24.
11. Lodhia KA, Gao S, Aleksic T, Esashi F, and Macaulay VM, Suppression of homologous recombination sensitizes human tumor cells to IGF-1R inhibition. *Int J Cancer.* **2015**;136:2961-6.
12. Blackford AN and Jackson SP, ATM, ATR, and DNA-PK: The Trinity at the Heart of the DNA Damage Response. *Mol Cell.* **2017**;66:801-817.
13. Aleksic T, Gray N, Wu X, Rieunier G, Osher E, Mills J *et al.*, Nuclear IGF1R Interacts with Regulatory Regions of Chromatin to Promote RNA Polymerase II Recruitment and Gene Expression Associated with Advanced Tumor Stage. *Cancer Res.* **2018**;78:3497-3509.
14. Kotsantis P, Silva LM, Irmscher S, Jones RM, Folkes L, Gromak N *et al.*, Increased global transcription activity as a mechanism of replication stress in cancer. *Nat Commun.* **2016**;7:13087.
15. Friedbichler K, Hofmann MH, Kroez M, Ostermann E, Lamche HR, Koessl C *et al.*, Pharmacodynamic and antineoplastic activity of BI 836845, a fully human IGF ligand-neutralizing antibody, and mechanistic rationale for combination with rapamycin. *Mol Cancer Ther.* **2014**;13:399-409.
16. Lukas C, Savic V, Bekker-Jensen S, Doil C, Neumann B, Pedersen RS *et al.*, 53BP1 nuclear bodies form around DNA lesions generated by mitotic transmission of chromosomes under replication stress. *Nat Cell Biol.* **2011**;13:243-53.
17. Zeman MK and Cimprich KA, Causes and consequences of replication stress. *Nat Cell Biol.* **2014**;16:2-9.

18. Conti C, Sacca B, Herrick J, Lalou C, Pommier Y, and Bensimon A, Replication fork velocities at adjacent replication origins are coordinately modified during DNA replication in human cells. *Mol Biol Cell*. **2007**;18:3059-67.
19. Ma M, Rodriguez A, and Sugimoto K, Activation of ATR-related protein kinase upon DNA damage recognition. *Curr Genet*. **2020**;66:327-333.
20. Chabes A and Thelander L, Controlled protein degradation regulates ribonucleotide reductase activity in proliferating mammalian cells during the normal cell cycle and in response to DNA damage and replication blocks. *J Biol Chem*. **2000**;275:17747-53.
21. Creighton CJ, Casa A, Lazard Z, Huang S, Tsimelzon A, Hilsenbeck SG *et al.*, Insulin-like growth factor-I activates gene transcription programs strongly associated with poor breast cancer prognosis. *J Clin Oncol*. **2008**;26:4078-85.
22. Kim EK and Choi EJ, Compromised MAPK signaling in human diseases: an update. *Arch Toxicol*. **2015**;89:867-82.
23. D'Angiolella V, Donato V, Forrester FM, Jeong YT, Pellacani C, Kudo Y *et al.*, Cyclin F-mediated degradation of ribonucleotide reductase M2 controls genome integrity and DNA repair. *Cell*. **2012**;149:1023-34.
24. de Bono J, Lin CC, Chen LT, Corral J, Michalarea V, Rihawi K *et al.*, Two first-in-human studies of xentuzumab, a humanised insulin-like growth factor (IGF)-neutralising antibody, in patients with advanced solid tumours. *Br J Cancer*. **2020**;122:1324-1332.
25. Pike KG, Barlaam B, Cadogan E, Campbell A, Chen Y, Colclough N *et al.*, The Identification of Potent, Selective, and Orally Available Inhibitors of Ataxia Telangiectasia Mutated (ATM) Kinase: The Discovery of AZD0156 (8-{6-[3-(Dimethylamino)propoxy]pyridin-3-yl}-3-methyl-1-(tetrahydro-2 H-pyran-4-yl)-1,3-dihydro-2 H-imidazo[4,5- c]quinolin-2-one). *J Med Chem*. **2018**;61:3823-3841.
26. Bueno RC, Canevari RA, Villacis RA, Domingues MA, Caldeira JR, Rocha RM *et al.*, ATM down-regulation is associated with poor prognosis in sporadic breast carcinomas. *Ann Oncol*. **2014**;25:69-75.
27. Kim Y, Han D, Min H, Jin J, Yi EC, and Kim Y, Comparative proteomic profiling of pancreatic ductal adenocarcinoma cell lines. *Mol Cells*. **2014**;37:888-98.
28. Sanderson MP, Hofmann MH, Garin-Chesa P, Schweifer N, Wernitznig A, Fischer S *et al.*, The IGF1R/INSR Inhibitor BI 885578 Selectively Inhibits Growth of IGF2-Overexpressing Colorectal Cancer Tumors and Potentiates the Efficacy of Anti-VEGF Therapy. *Mol Cancer Ther*. **2017**;16:2223-2233.
29. Smida M, Fece de la Cruz F, Kerzendorfer C, Uras IZ, Mair B, Mazouzi A *et al.*, MEK inhibitors block growth of lung tumours with mutations in ataxia-telangiectasia mutated. *Nat Commun*. **2016**;7:13701.
30. Wang C, Jette N, Moussienko D, Bebb DG, and Lees-Miller SP, ATM-Deficient Colorectal Cancer Cells Are Sensitive to the PARP Inhibitor Olaparib. *Transl Oncol*. **2017**;10:190-196.
31. Dunlop CR, Wallez Y, Johnson TI, Bernaldo de Quiros Fernandez S, Durant ST, Cadogan EB *et al.*, Complete loss of ATM function augments replication catastrophe induced by ATR inhibition and gemcitabine in pancreatic cancer models. *Br J Cancer*. **2020**;123:1424-1436.
32. Rybaczek D, Musialek MW, and Balcerzyk A, Caffeine-Induced Premature Chromosome Condensation Results in the Apoptosis-Like Programmed Cell Death in Root Meristems of *Vicia faba*. *PLoS One*. **2015**;10:e0142307.
33. Toledo LI, Altmeyer M, Rask MB, Lukas C, Larsen DH, Povlsen LK *et al.*, ATR prohibits replication catastrophe by preventing global exhaustion of RPA. *Cell*. **2013**;155:1088-103.
34. Putluri N, Maity S, Kommagani R, Creighton CJ, Putluri V, Chen F *et al.*, Pathway-centric integrative analysis identifies RRM2 as a prognostic marker in breast cancer associated with poor survival and tamoxifen resistance. *Neoplasia*. **2014**;16:390-402.



35. Rasmussen RD, Gajjar MK, Tuckova L, Jensen KE, Maya-Mendoza A, Holst CB *et al.*, BRCA1-regulated RRM2 expression protects glioblastoma cells from endogenous replication stress and promotes tumorigenicity. *Nat Commun.* **2016**;7:13398.
36. He Z, Hu X, Liu W, Dorrance A, Garzon R, Houghton PJ *et al.*, P53 suppresses ribonucleotide reductase via inhibiting mTORC1. *Oncotarget.* **2017**;8:41422-41431.
37. Pfister SX, Markkanen E, Jiang Y, Sarkar S, Woodcock M, Orlando G *et al.*, Inhibiting WEE1 Selectively Kills Histone H3K36me3-Deficient Cancers by dNTP Starvation. *Cancer Cell.* **2015**;28:557-568.
38. Yoshida Y, Tsunoda T, Doi K, Tanaka Y, Fujimoto T, Machida T *et al.*, KRAS-mediated up-regulation of RRM2 expression is essential for the proliferation of colorectal cancer cell lines. *Anticancer Res.* **2011**;31:2535-9.
39. Waraky A, Lin Y, Warsito D, Haglund F, Aleem E, and Larsson O, Nuclear insulin-like growth factor 1 receptor phosphorylates proliferating cell nuclear antigen and rescues stalled replication forks after DNA damage. *J Biol Chem.* **2017**;292:18227-18239.
40. Yang C, Zhang Y, Chen Y, Ragaller F, Liu M, Corvigno S *et al.*, Nuclear IGF1R interact with PCNA to preserve DNA replication after DNA-damage in a variety of human cancers. *PLoS One.* **2020**;15:e0236291.
41. Bester AC, Roniger M, Oren YS, Im MM, Sarni D, Chaoat M *et al.*, Nucleotide deficiency promotes genomic instability in early stages of cancer development. *Cell.* **2011**;145:435-46.
42. Vafa O, Wade M, Kern S, Beeche M, Pandita TK, Hampton GM *et al.*, c-Myc can induce DNA damage, increase reactive oxygen species, and mitigate p53 function: a mechanism for oncogene-induced genetic instability. *Mol Cell.* **2002**;9:1031-44.
43. Aird KM, Zhang G, Li H, Tu Z, Bitler BG, Garipov A *et al.*, Suppression of nucleotide metabolism underlies the establishment and maintenance of oncogene-induced senescence. *Cell Rep.* **2013**;3:1252-65.
44. Kelsall IR, Langenick J, MacKay C, Patel KJ, and Alpi AF, The Fanconi anaemia components UBE2T and FANCM are functionally linked to nucleotide excision repair. *PLoS One.* **2012**;7:e36970.
45. Peretz S, Jensen R, Baserga R, and Glazer PM, ATM-dependent expression of the insulin-like growth factor-I receptor in a pathway regulating radiation response. *Proc Natl Acad Sci U S A.* **2001**;98:1676-81.
46. Smith GC, d'Adda di Fagagna F, Lakin ND, and Jackson SP, Cleavage and inactivation of ATM during apoptosis. *Mol Cell Biol.* **1999**;19:6076-84.
47. Yi R, Lin A, Cao M, Xu A, Luo P, and Zhang J, ATM Mutations Benefit Bladder Cancer Patients Treated With Immune Checkpoint Inhibitors by Acting on the Tumor Immune Microenvironment. *Front Genet.* **2020**;11:933.
48. Khoronenkova SV and Dianov GL, ATM prevents DSB formation by coordinating SSB repair and cell cycle progression. *Proc Natl Acad Sci U S A.* **2015**;112:3997-4002.
49. Aird KM, Worth AJ, Snyder NW, Lee JV, Sivanand S, Liu Q *et al.*, ATM couples replication stress and metabolic reprogramming during cellular senescence. *Cell Rep.* **2015**;11:893-901.
50. Pefani DE, Latusek R, Pires I, Grawenda AM, Yee KS, Hamilton G *et al.*, RASSF1A-LATS1 signalling stabilizes replication forks by restricting CDK2-mediated phosphorylation of BRCA2. *Nat Cell Biol.* **2014**;16:962-71, 1-8.

## Legends to Figures

**Figure 1. IGF-1R inhibition induces replication stress.** **A.** MCF7 cells were xentuzumab-treated for 5 days, showing representative immunofluorescence for  $\gamma$ H2AX (scale bar 10 $\mu$ m). Graph: mean  $\pm$  SEM foci ( $n \geq 50$  nuclei). **B.** Serum-starved MCF7 cells were xentuzumab-treated as A and with 50nM IGF-1 in final 15min. **C.** MCF7 cells were treated as A showing representative immunofluorescence for 53BP1 bodies (scale bar 10 $\mu$ m). Graph below: mean  $\pm$  SEM 53BP1 bodies ( $n \geq 50$  nuclei). **D.** Cyclin A and 53BP1 immunofluorescence in MCF7 cells xentuzumab-treated (100nM) as A, or 72h post-siRNA transfection (scale 10 $\mu$ m, white arrows: cyclin A negative cells). Western blot below confirms IGF-1R depletion. Graph: mean  $\pm$  SEM 53BP1 bodies. **E.** Replication tract images in MCF7 cells 72h after siRNA transfection. Graph to right: tract length (CldU+IdU) in MCF7 cells 48-120h after siRNA-transfection, re-transfecting 96h and 120h time-points at 72h. Red line: median. **F, G.** MCF7 cells transfected with Control (siCtrl) or 3 different IGF-1R siRNAs, processed after 72h for DNA fiber analysis, showing tract length (F), fork speed (G). **H, I.** DNA fiber analysis in MCF7 cells treated with PBS (control) or 1  $\mu$ M xentuzumab for 6h, showing tract length (H), fork speed (I). **J.** DNA fiber analysis comparing sister fork ratios. Left panel: representative sister forks from MCF7 cells 72h post-siRNA transfection. Right: sister fork ratios (median, lower/upper quartiles, minimum/maximum values).

**Figure 2. IGF-1R depletion activates ATR-CHK1 and intra-S checkpoint.** **A.** MCF7 cells were siRNA transfected, harvested after 48-120h for western blot for phospho-S345 and total CHK1. Cells were re-transfected with siRNAs at 72h. **B.** MCF7 cells were siRNA transfected as A and after 72h were processed for DNA fiber analysis to quantify newly-fired origins. Upper panel: two types of newly-fired origins (arrows, direction of fork progression). Graph below, newly-fired origins quantified as green tracts only and red tracts with bilateral green extension expressed as % of total tracts ( $n=200$  per condition). **C-D.** MCF7 cells were siRNA-transfected, the following day treated with nocodazole,

after 18h released into nocodazole-free medium and collected after 0-24h for cell cycle analysis (n=3 independent experiments).

**Figure 3. IGF-1R regulates RNR activity via AKT, MEK-ERK and JUN.** **A.** MCF7 cells were siRNA-transfected and after 48h harvested for dNTP assay. Graph: mean  $\pm$  SEM fold-change in dATP content (n=3 independent assays). **B.** HCT15 cells were siRNA-transfected and dNTPs were extracted and assayed as A. Graph: mean  $\pm$  SEM fold-change in dNTP content (n=3 independent assays). **C.** Serum-starved MCF7 cells IGF-treated for 24h, *RRM2* mRNA assessed by qPCR (mean  $\pm$  SEM of 3 independent analyses). **D.** Serum-starved MCF7 cells pre-treated with 1 $\mu$ M xentuzumab for 2h then xentuzumab with 50nM IGF-1 for 24h. Graph to right: mean  $\pm$  SEM *RRM2* protein (n=3 independent blots, corrected for  $\beta$ -tubulin, expressed as % of levels in serum-starved cells). **E, F.** MCF7 cells were siRNA transfected, collected after 48h for: E, western blot, graph shows mean  $\pm$  SEM *RRM2* protein (n=3 western blots expressed as % of siControl); F, qPCR for *RRM2* mRNA (mean  $\pm$  SEM of 3 independent analyses). **G.** Breast cancer cells were transfected with Control (siCtrl) or IGF-1R siRNAs and lysed after 48h for western blot to assess IGF-1R depletion and *RRM2* expression. **H-I.** Serum-starved MCF7 cells treated with IGF-1 alone or with 10nM MEK inhibitor (MEKi) trametinib (H) or 3.5mM AKT inhibitor (AKTi) AZD5363 (I). Graphs to right: quantification of *RRM2* from 3 independent blots in each case. **J.** MCF7 cells transfected with siIGF-1R and/or siJUN were analysed by western blot, with similar results in a second independent blot. Graph: quantification (mean  $\pm$  range), showing reduction in *RRM2* protein to 67 $\pm$ 0.5% of siControl levels with siJUN\_1 and 72 $\pm$ 17 % with siJUN\_2; **K.** Left: schematic of *RRM2* promoter reporter showing JUN consensus binding motif TGACTCA. Right: luciferase assay after transient transfection with *RRM2* promoter luciferase reporter (n=3 assays each with triplicate technical replicates).

**Figure 4. RRM2 overexpression rescues IGF-1R depleted or inhibited cells from replication stress.**

**A-B.** U2OS cells stably-transfected with *RRM2* or empty vector (EV) were analysed by western blot

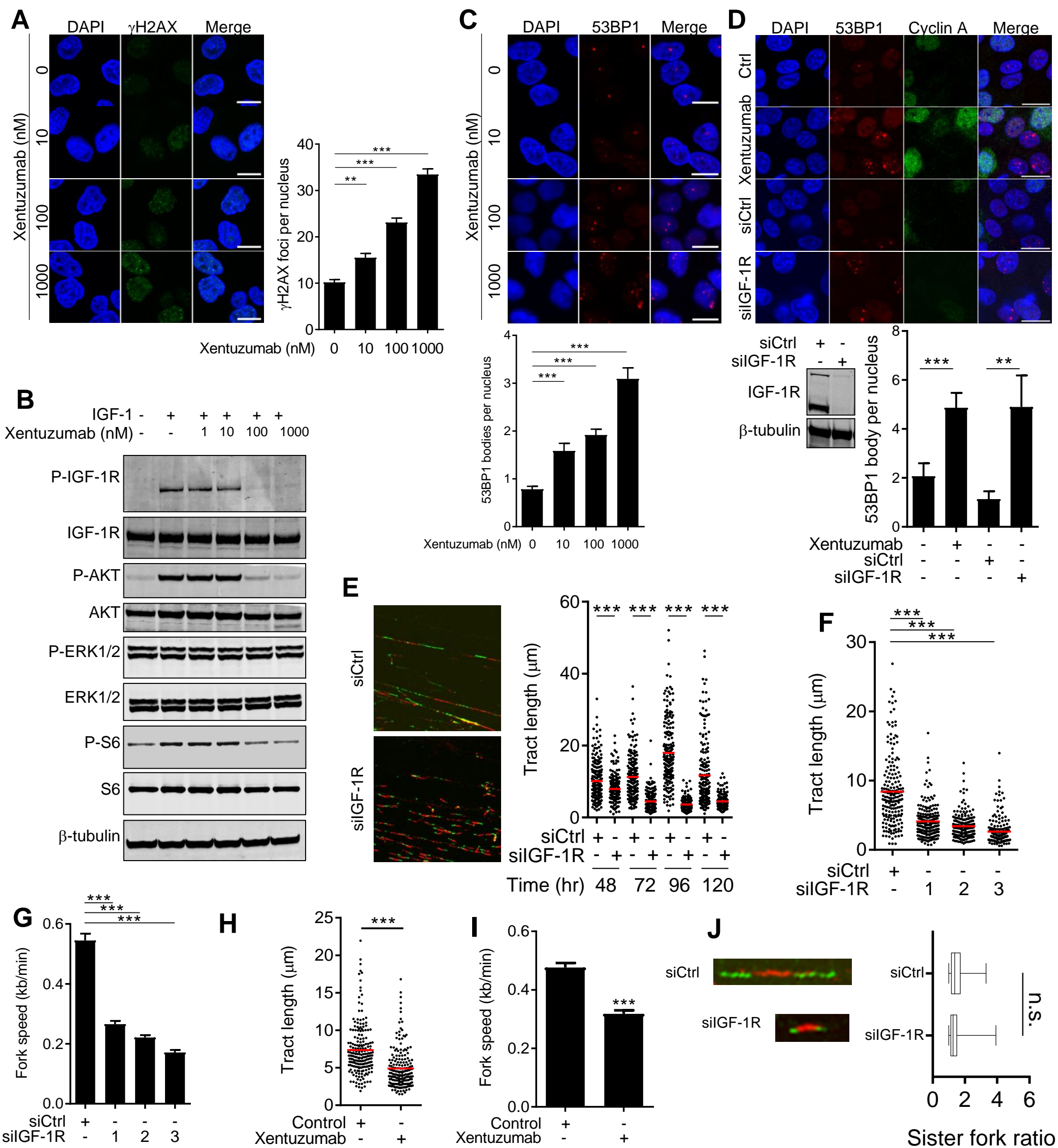
48h after IGF- 1R siRNA transfection (A) or 72h treatment with 100nM xentuzumab (B). **C.** Parallel cultures siRNA-transfected as A were processed for 53BP1 immunofluorescence (scale 10 $\mu$ m). Graph below: mean  $\pm$  SEM 53BP1 bodies (n=30 nuclei). **D-E.** MCF7 cells stably transfected with empty vector (EV) or RRM2 cDNA were harvested 48h after transfection with siControl or siIGF-1R for D, western blot, E. DNA fiber analysis showing: left, representative images; right, quantification of tract length (n=200). **F.** Stably-transfected MCF7 cells were treated with xentuzumab for 72h and processed as C for 53BP1 immunofluorescence (scale 10 $\mu$ m). Graph to right: mean  $\pm$  SEM 53BP1 bodies (n $\geq$ 20 nuclei).

**Figure 5. ATM maintains viability in the context of xentuzumab-induced replication stress. A.**

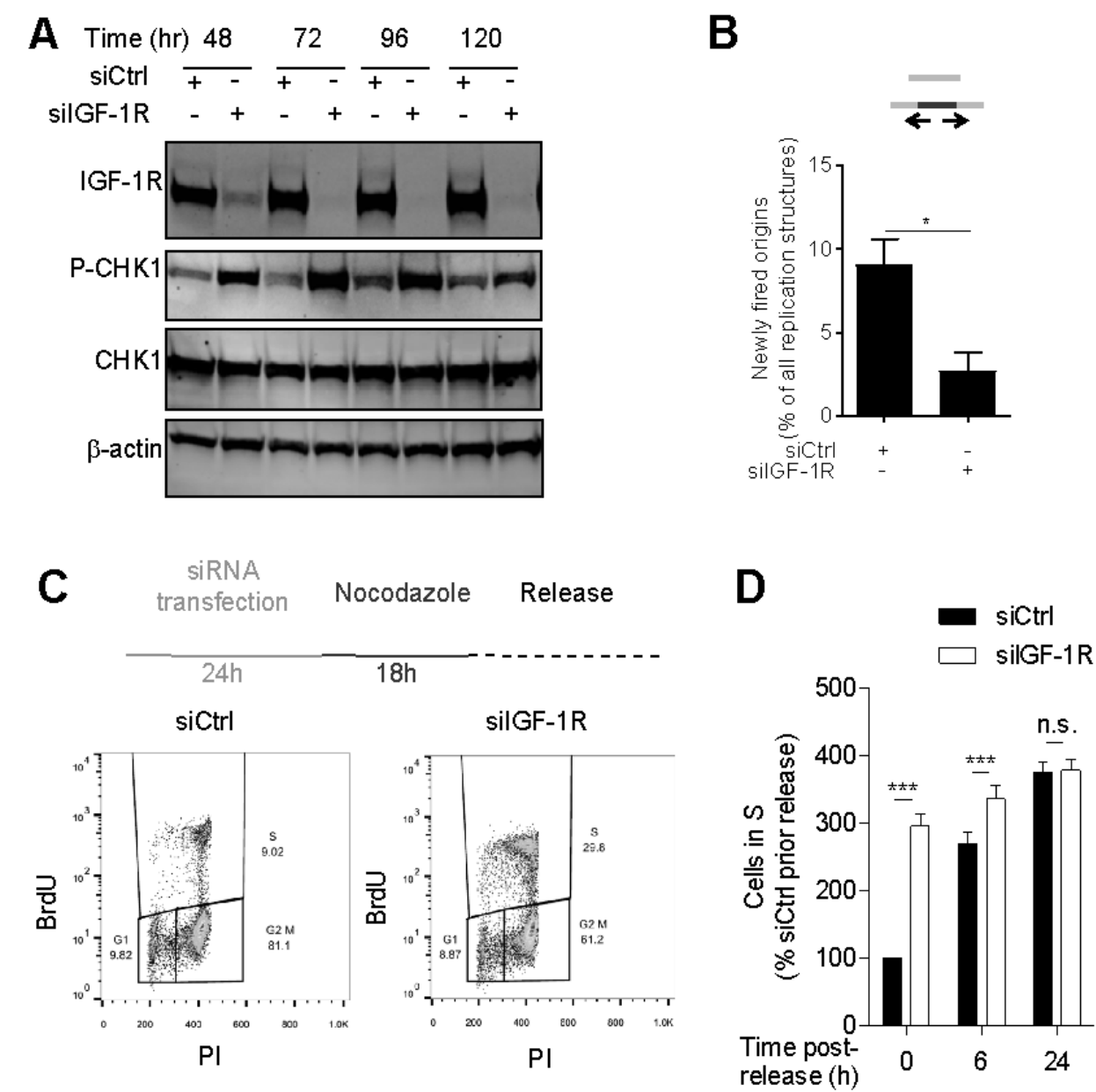
Relative viability after 5 days treatment with 1 $\mu$ M xentuzumab. **B.** MCF7 cells treated with 1  $\mu$ M xentuzumab alone or with 60 compounds at 0.1, 1 and 10  $\mu$ M, viability measured after 5 days. Correlation between duplicate screens was 0.97, and screen Z-Factors calculated using positive control for viability inhibition (PLK1 inhibitor BI-2536) were 0.64 at 100 nM, 0.68 at 1  $\mu$ M and 0.72 at 10  $\mu$ M, indicating high-quality screens. Graph: compounds screened at 0.1 mM, ranked by ratio of log<sub>10</sub> compound alone/ compound+xentuzumab. Green box: top 12 compounds inducing at least additive effects (log<sub>10</sub> ratio>0). Venn diagram: top-ranked hits in common at 0.1, 1 and 10  $\mu$ M compound (also see Supplemental Figure S4A). **C.** MCF7 viability treated for 5 days with KU-55933 alone/with 1 $\mu$ M xentuzumab. **D.** MCF7 cells pre-treated with 10 $\mu$ M KU-55933 and/or xentuzumab for 72h, analysed 30 min after 5Gy irradiation. **E.** Combination indices (CI) calculated from viability data. CI values <0.8 indicate synergy and <0.3, strong synergy. **F-G.** Cell death measured in MCF7 cells as PI-positive cells as % of total (Hoechst-positive) cells, expressed relative to solvent-treated controls (representative color images in Suppl Figure S5A); MCF7 cells were treated for 5 days with 1 $\mu$ M xentuzumab and KU-55933 or AZD0156. Cells were stained with PI (dead cells)/Hoechst (total nuclei) and % cell death was quantified on the Celigo Imaging Cytometer.

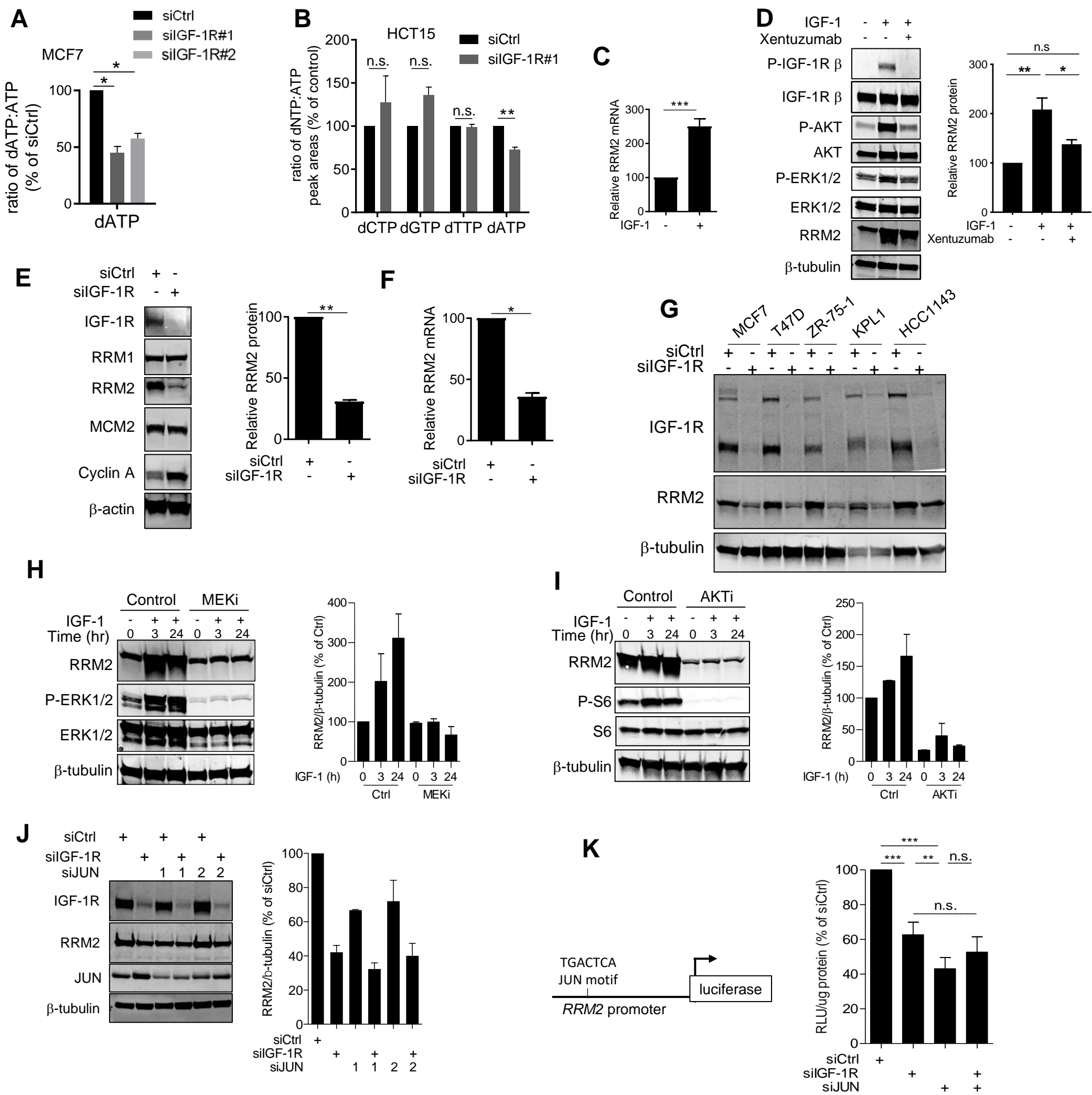
**Figure 6. ATM loss sensitizes to IGF inhibition.** **A.** Pan-cancer analysis (926 cell lines) associating *ATM* homozygous mutations and sensitivity to IGF-1R inhibitor BMS-754807 (cancerxgene.org). **B.** *ATM*<sup>+/+</sup> and *ATM*<sup>-/-</sup> fibroblasts treated with 188 kinase inhibitors (1μM), viability measured after 3 days, compounds ranked by ratio of log10 viability. Green box: top-ranked compounds, top hit arrowed. **C.** Fibroblasts as B treated with BI-885578, viability measured after 5 days. Blot to right: serum-starved fibroblasts treated with BI-885578 for 24h and in final 15 min with IGF-1. **D.** Viability of CRC cells treated with xentuzumab or BI-885578 for 5 days. Blot confirms *ATM* null status of SK-CO-1. **E-F.** Mice bearing SK-CO-1 xenografts were treated twice weekly (arrows) with solvent or xentuzumab showing E: representative tumor-bearing mice, F: tumor volumes. **G.** Immunohistochemical (IHC) analysis of SK-CO-1 tumors and mouse skin (scale 100μm). H-scores for RRM2 and BrdU represent moderate-strong (2-3+) staining. There was less striking reduction in RRM2 and BrdU when including weak (1+) positivity (Supplementary Figure S6I-J), consistent with S phase arrest induced in MCF7 cells by IGF-1R depletion (Supplementary Figure S1G). *ATM* null status of SK-CO-1 xenografts was confirmed by IHC (Supplementary Figure S6H), mouse epidermis acting as positive control for *ATM*. **H.** *ATM* proficient or deficient MiaPaCa2 PDAC spheroids were treated with solvent or xentuzumab. Spheroid size was measured every 1-3 days and expressed relative to spheroid size immediately prior to treatment. **I.** *ATM* proficient MiaPaCa2 spheroids were treated with AZD0156 and/or xentuzumab and spheroid size measured as H.

**Figure 7. Tolerable ssDNA lesions in IGF-1R deficient cells are converted to DSBs by *ATM* loss.** **A.** CRC cells were siRNA-transfected, collected at 48h for DNA fiber analysis. **B.** Immunofluorescence in MCF7 cells 72h after treatment with xentuzumab (100nM) and/or AZD0156 (1μM). Graph: mean ± SEM 53BP1 bodies (n≥70 nuclei per condition). **C-D.** MCF7 cells treated with 1μM xentuzumab and/or 10μM KU-55933, after 72h processed for: C alkaline comet assay; G, neutral comet assay. Left: representative images, right: quantification of % tail DNA (n=100 comets per condition).

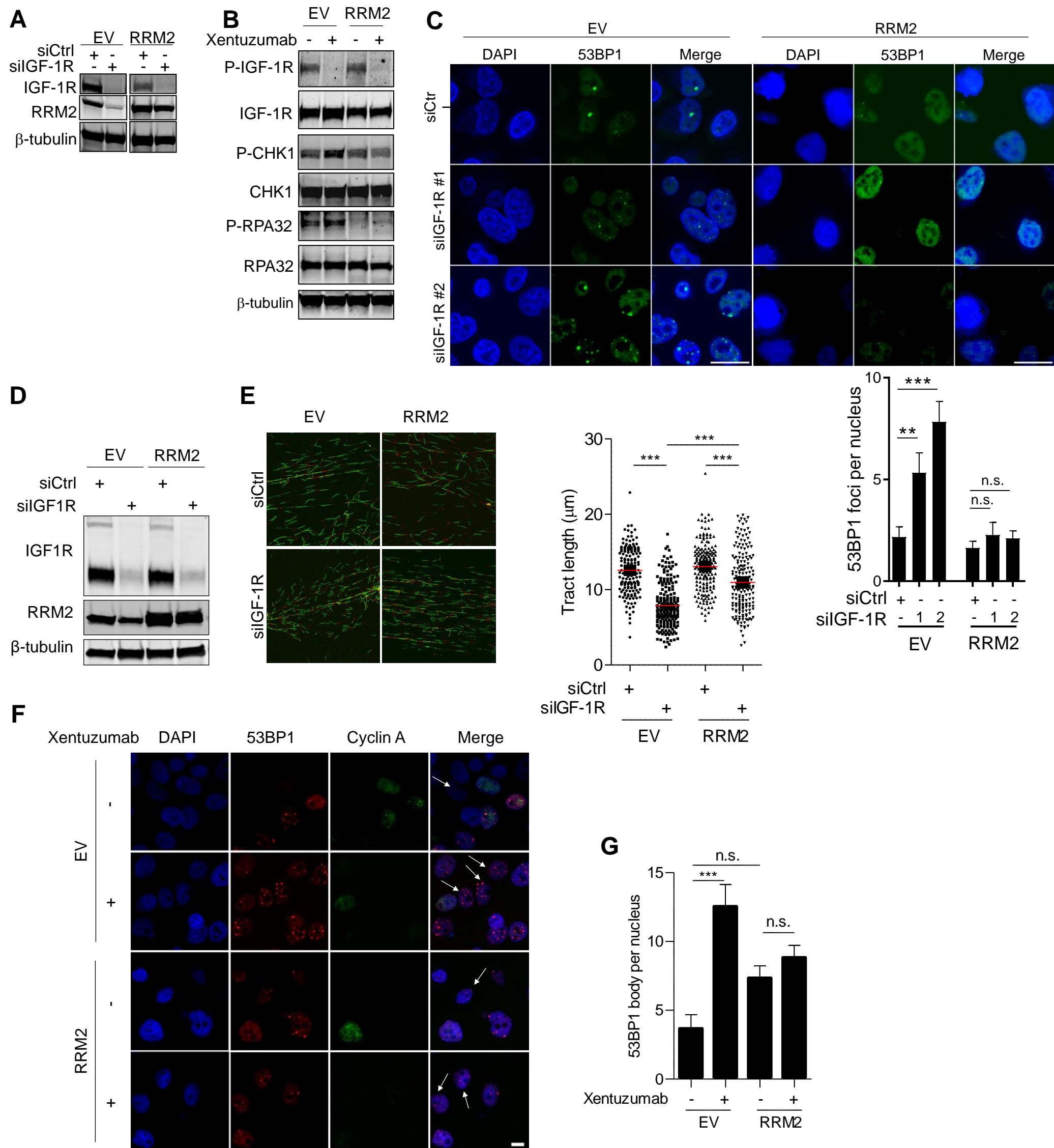
**Figure 1**

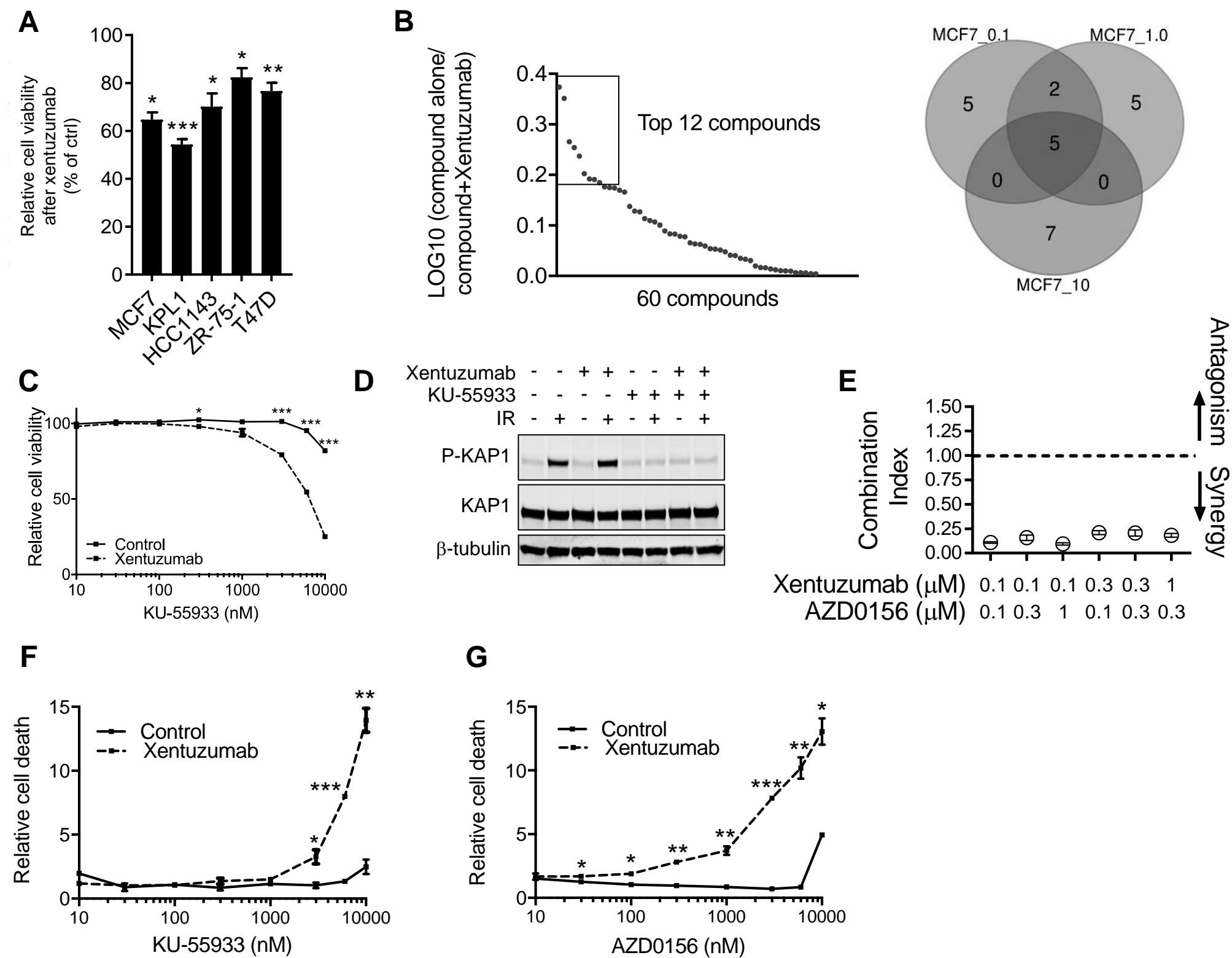
**Figure 2**

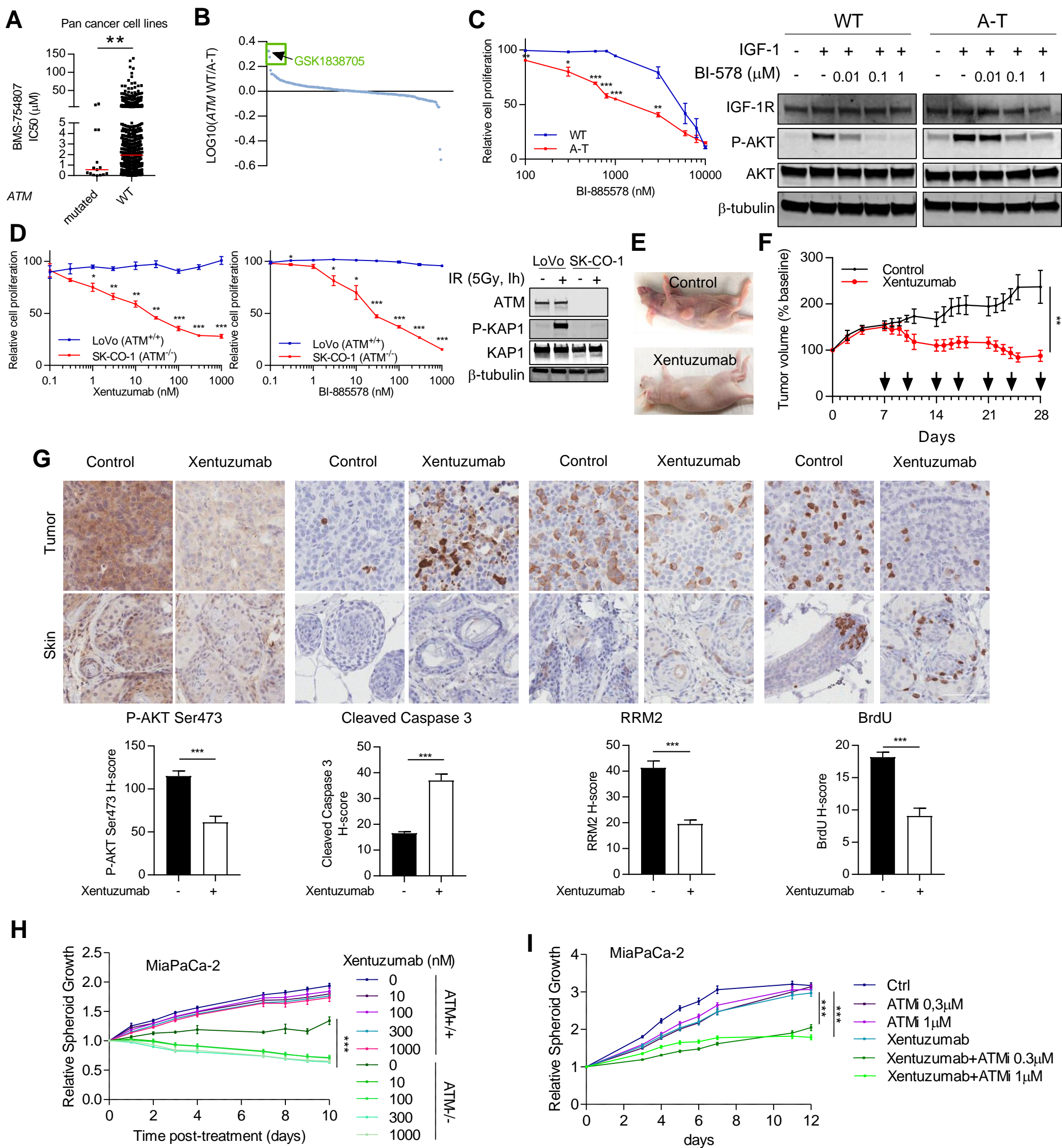


**Figure 3**



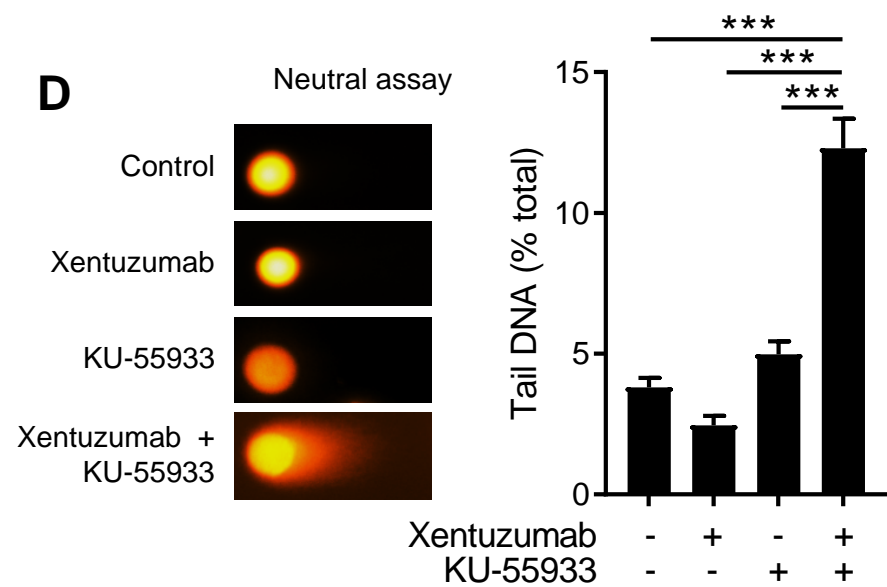
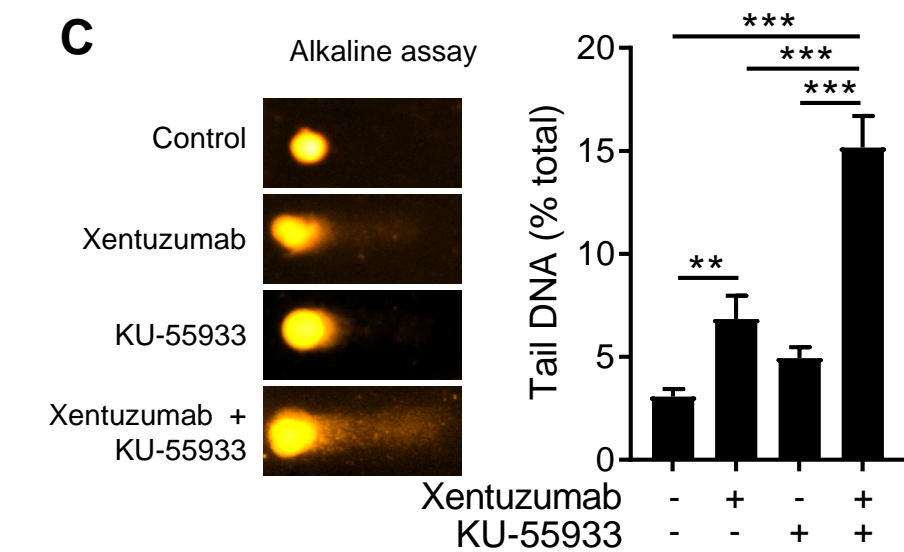
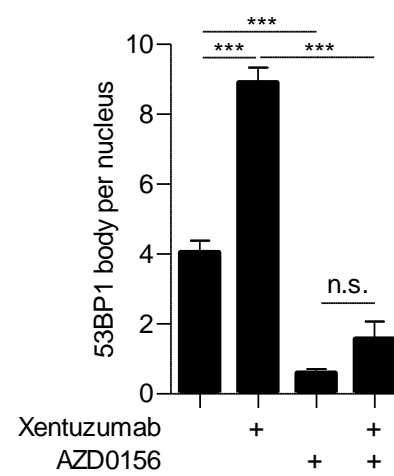
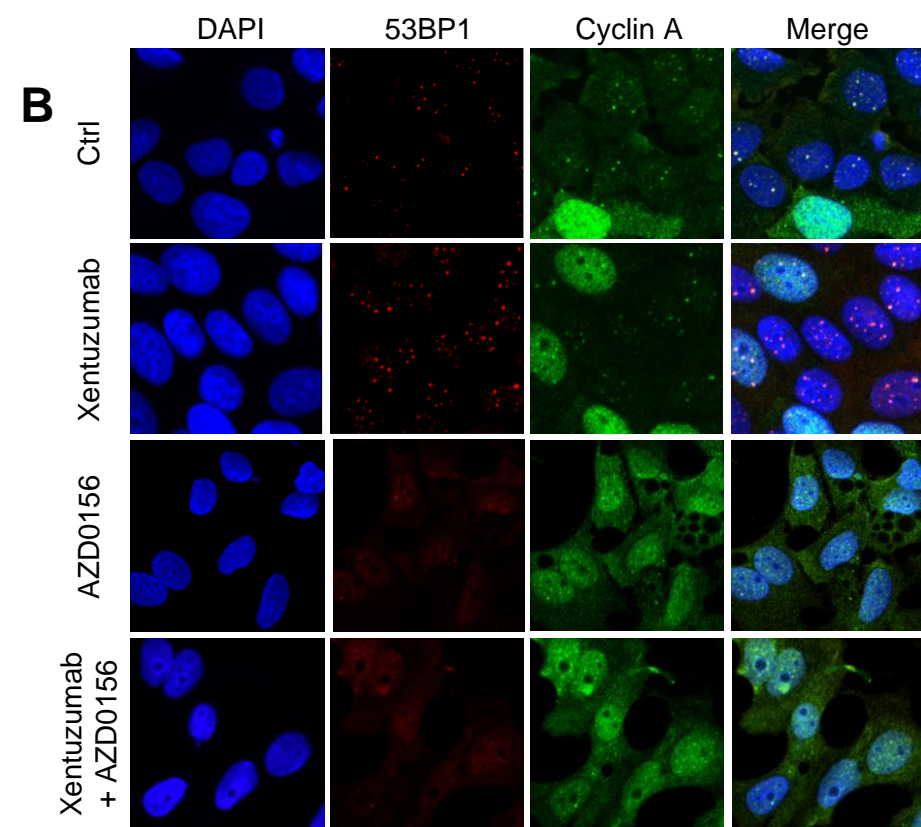
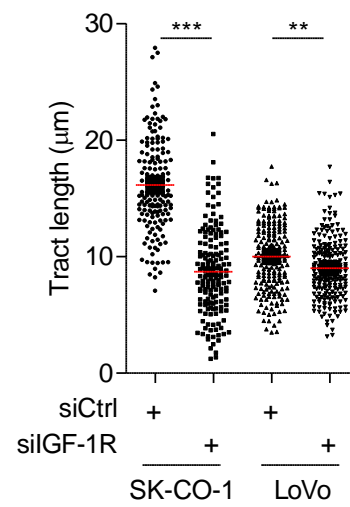
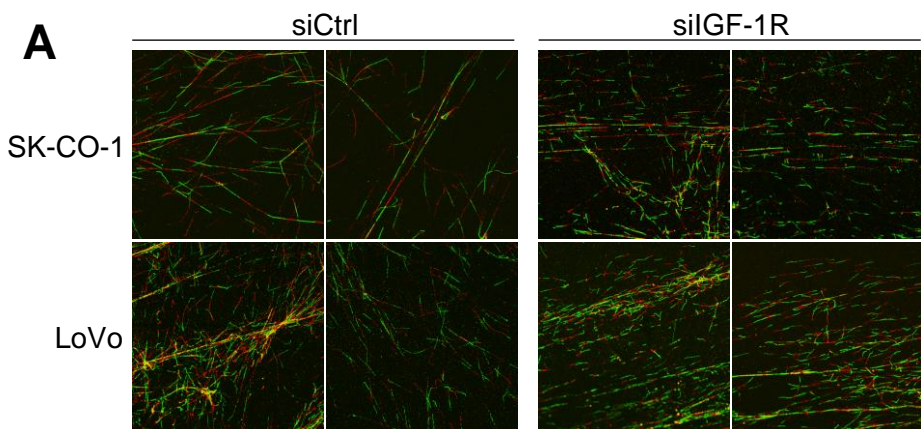
**Figure 4**

**Figure 5**

**Figure 6**



**Figure 7**



## Supplementary methods

**Cell cultures and reagents.** Cells were cultured in DMEM (Thermo Fisher Scientific) supplemented with 10% fetal calf serum (FCS) (Invitrogen), penicillin (100 units/mL) and streptomycin (0.1mg/mL; Invitrogen) at 37°C in a humidified incubator with 5% CO<sub>2</sub>. Xentuzumab and BI-885578 were from Boehringer Ingelheim, other inhibitors as follows: KU-55933 (Bio-Techne; R&D systems), trametinib and AZD0156 (Selleck), AZD5363 and 60 drug custom library (Strattech Scientific), 188 compound kinase chemogenomic set (KCGS, Structural Genomics Consortium; [www.sgc-unc.org/kinase-chemogenomics](http://www.sgc-unc.org/kinase-chemogenomics)). Cells were transfected with 50 nM IGF-1R siRNAs from Qiagen, Cell Signaling Technology or generated in-house (1) or with AllStars Negative Control siRNA (Qiagen), using Oligofectamine (Invitrogen) as described in (2).

**Cell viability, doubling time, spheroid and cell death assays.** Cells seeded in 96 well plates were treated with drug(s) and after 5 days underwent viability assay (CellTiter-Blue, Promega) measuring fluorescence (570nm) on a POLARstar Omega microplate reader (BMG Labtech). Viability data were used to calculate Combination Indices using ComboSyn software following the Chou-Talalay method (3). Doubling time was measured by counting cells on a daily basis for 5 days and analysing the linear part of the growth curve (number of cells versus time) using the equation  $(t_2 - t_1) / 3,32 \times (\log n_2 - \log n_1)$  where t is time and n number of cells, as described in (4). For 3D assays, cells were seeded in Ultra-low attachment 96-well plates (Corning) and after 24 hr incubation spheroids were treated with solvent or drug(s) and imaged every 1-3 days on the GelCount (Oxford Optronix). For death assay, cells were stained with 1mg/ml Hoechst 33342 and 4 µM propidium iodide (PI) to quantify total and dead cells on a Celigo Imaging Cytometer (Nexcelom).

**Western blotting** was performed as previously (5). Bound primary antibodies (Supplementary Table S1) were detected by secondary antibodies coupled to IRDye (LI-COR), visualised using the Odyssey Quantitative Fluorescence Imaging System, and band intensities were quantified using Odyssey software.

**Immunofluorescence.** Cells were seeded and treated in 4-well Labtek plates and were fixed for 10 min in 4% paraformaldehyde (PFA), washed in PBS and permeabilized for 5 min in PBS 0.1% Triton/4% FCS. Cells were washed in PBS, blocked for 1h in 10% BSA, washed in PBS and incubated with primary antibodies (Supplementary Table S1) for 1h at RT. Cells were washed in PBS, incubated with secondary antibodies for 1h at RT in the dark. Slides were air-dried and mounted in VectaShield (H1200, Vector Laboratories) with DAPI. Images acquisitions were performed using an inverted laser scanning confocal LSM 710 microscope UV Zeiss equipped with x63 and x40 oil objectives. Images were processed with the Zeiss software (Zen), imported to ImageJ, pseudocolored and merged.

**DNA fiber assays** were performed as described (6, 7). Briefly, cultures in exponential growth were incubated with CldU (25 µM, Sigma, C6891) for 20 min. Cells were washed 3 times in warm PBS and incubated in medium containing IdU (250 µM, Sigma, I7125) for 20 min. Cells were lysed and nuclei were spread onto glass slides in spreading buffer (200 mM Tris-HCl pH 7.4, 50 mM EDTA, 0.5% SDS). Slides were slightly tilted to allow DNA to spread slowly on the whole length of the slide, and then air dried and fixed with methanol/acetic acid (3:1) for 10min. To detect incorporation of CldU/IdU, slides were washed in PBS, DNA was denatured in 2.5 M HCl (1 h, RT) and blocked in 2% BSA+ 0.1% Tween and incubated (overnight, 4°C) with mouse anti-IdU antibody and rat anti-CldU in blocking solution. Slides were washed 5 times in PBS+Tween 0.2%, briefly rinsed in blocking solution and incubated (1 h, RT) with anti-mouse Alexa Fluor 488 and anti-rat Alexa Fluor 594 antibodies in blocking solution. Slides were washed 5 times in PBS+Tween 0.2% and mounted in Vectashield. Image acquisitions were performed using an inverted laser scanning confocal LSM 710 microscope UV Zeiss equipped with x63

oil objective. Images were processed with the Zeiss software (Zen), imported to ImageJ, pseudocolored and merged. Fork velocity was converted to kb/min based on the tract length ( $\mu\text{m}$ ) and the duration of CldU/IdU incubation (20min each).

**Flow cytometry:** Following siRNA transfection and nocodazole treatment (Sigma-Aldrich M1404, 60ng/mL), cultures in exponential growth were pulsed with BrdU (20 $\mu\text{M}$ , Invitrogen) for 30 min. Monolayer and suspension cells were collected and processed as in (8, 9). In brief, cells were fixed in 70% ethanol for 30 min, denatured in 2M HCl containing 0.1 mg/mL pepsin for 20 min. After washes with PBS and 2% FCS, cells were incubated with primary anti-BrdU antibody (1:500, BD Bioscience, 347580) overnight at 4°C. After washes with PBS and 2% FCS, cells were incubated with secondary antibody anti-mouse Alexa Fluor 488 (1/500, Molecular Probes) for 1h at RT. After PBS washes, cells were resuspended in 0.1 mg/ml PI. Fluorescence was analysed using a FACSCalibur instrument (BD Biosciences), and results were analyzed with FlowJo software (v.10).

**Nucleotide quantification.** Cells were harvested and nucleotides extracted with 70% ice-cold methanol. Precipitated proteins were removed by centrifugation, supernatants were stored at  $-80^{\circ}\text{C}$  then dried in a heated vacuum centrifuge and reconstituted in HPLC starting eluent. Determination of the dNTP pool size was performed by HPLC as described in (10).

**Quantitative PCR:** RNAs were extracted and reverse transcribed using the Pure Link RNA Mini RNA extraction kit (Ambion) and SuperScript III First-Strand Synthesis SuperMix (Invitrogen). The cDNAs were amplified using primers RRM1 F (AAACGCCATCGCCCCATTGGAA), RRM1 R (ACAGCTGGCTTCCAGAGCACCATA), RRM2 F (TTTAAAGGCTGCTGGAGTGAGG), RRM2 R (GCAGCTGCTTTAGTTTTCGGCT),  $\beta$ -actin F (AGGATTCTATGTGGGCGAC) and  $\beta$ -actin R (ATAGCACAGCCTGGATAGCAA) and Sybr Green PCR Mix (Applied Biosystems) on a 7500 Fast RT-PCR System (Applied Biosystems).

**Luciferase Assays:** ONE-Glo<sup>TM</sup> EX Luciferase assay (Promega Cat. No. E8110) was used for testing of the effects of IGF-1R, c-JUN and E2F1 knockdown on RRM2 transcription levels. Briefly, MCF7 cells were seeded to be 70% confluent for transfection, then transfected with the RRM2 promoter reporter construct using Lipofectamine 3000<sup>TM</sup> (Invitrogen Cat. No. L3000008) as per the manufacturer's instructions. Control wells were also transfected with only a constitutively expressed GFP plasmid as a transfection efficiency control. SiRNAs for IGF-1R, c-Jun and E2F1 or All-Stars control were transfected 24h later and, following overnight incubation at 37°C, cells were reseeded in triplicate into a 96-well plate. The following day cells were tested with ONE-Glo<sup>TM</sup> EX Luciferase assay reagent (Promega Cat. No. E8110). Briefly, treated cells and ONE-Glo<sup>TM</sup> EX Luciferase assay reagent were equilibrated to RT before addition of ONE-Glo<sup>TM</sup> EX Luciferase assay reagent in 1:1 ratio of reagent to medium. Cells were incubated in luciferase reagent for 5 mins, RT on a rocker and shielded from light, and luminescence was measured on a POLARstar Omega plate reader (BMG Labtech). The protein content of the lysate was then quantified by Pierce BCA protein assay (ThermoFisher Cat. No. 23225) and luciferase activity was expressed as relative light units per  $\mu\text{g}$  protein.

**Generation of MCF7 stably overexpressing RRM2:** To generate RRM2-overexpressing MCF7 cells, pcDNA 3.1 control plasmid (#V79520, Invitrogen) or pcDNA3.1 RRM2 plasmid (Addgene, Plasmid #13796) was transfected into MCF7 cells using Lipofectamine 3000 Reagent Kit (#L3000001, Thermo Fisher Scientific) following the manufacturer's instructions. MCF7 cells were cultured to 70% confluency. Lipofectamine 3000 reagent and P3000 reagent were diluted with Opti-MEM medium (#31985-047, Gibco) and then mixed with 2.5  $\mu\text{g}$  plasmid DNA. The transfection mix was added into cell culture medium for 48 hours. The cells were then cultured with medium containing 800  $\mu\text{g}/\text{mL}$

G418 (#G8186, Sigma-Aldrich) for 72 hours. The surviving colonies were picked and cultured with medium containing 800 µg/mL G418 for 30 days to obtain stably expressing cells. The expression level of RRM2 was determined by western blot analysis.

**Compound screens:** Two compound screens were performed, first to test xentuzumab with a targeted custom library in breast cancer cells, and secondly to test a library of kinase inhibitors in *ATM* WT MRC5-SV2 vs *ATM*<sup>-/-</sup> AT5BIVA fibroblasts. Duplicate screens were conducted in each case. For the breast cancer screen, 60 compounds were tested at 100 nM, 1 µM and 10 µM alone or in combination with 1 µM xentuzumab in MCF7, HCC1143, KPL1, T47D and ZR-75-1 cells. The cells were seeded at pre-optimised cell densities in 96-well plates by Perkin Elmer Janus liquid handling workstations. Cells were incubated for 24h at 37°C and treated with a drug library of 60 cell cycle, replication and DNA repair inhibitors alone or with 1 µM xentuzumab using the Perkin Elmer Janus liquid handling workstations. Cells were incubated for 5 days at 37°C followed by replacement of the medium by phenol-free DMEM containing 1mM resazurin (Cell Titer Blue, Promega). Cells were incubated for 2h at 37°C and fluorescence was read using EnVision multilabel plate reader (PerkinElmer). Screen replicate correlation was 0.97 and the screen Z-Factor calculated using the positive control for viability inhibition (PLK1 inhibitor BI-2536) was 0.64 at 100 nM, 0.68 at 1 µM and 0.72 at 10 µM, indicating a high-quality screen. The compound screen in *ATM* WT vs null fibroblasts used a 188-compound kinase chemogenomic set (KCGS), and viability was measured after 3 days as above. The screen Z-Factor calculated using the positive control for viability inhibition (camptothecin analogue SN-38) was 0.63 and 0.81 at 0.1 µM for *ATM* WT and mutated cells respectively, and 0.83 and 0.81 at 1 µM, indicating a high-quality screen.

**Single cell gel electrophoresis.** Alkaline comet assays were performed as in (11, 12). Briefly trypsinised cells were mixed with 1% low melting point agarose, spread onto glass slides on ice and flattened with cover slips. After solidification, cover slips were removed and slides were lysed in lysis buffer (2.5M NaCl, 100mM EDTA, 10mM Tris pH10.5, with *ex tempore* addition of 1% Triton X-100 and 1% DMSO) for 1h at 4°C. Slides were placed in an electrophoresis tank with fresh electrophoresis buffer (300mM NaOH, 1mM EDTA and 1% DMSO) for 40min to allow DNA unwinding. Slides were then subjected to electrophoresis for 25min at 25V, 300mA at RT. Slides were rinsed with neutralisation buffer (TrisHCl 500mM pH 8), stained with SyBr Gold (ThermoFisher) and stored at 4°C before image acquisition. For neutral comet assays, cells were agarose-embedded and spread on slides as above, and lysed in lysis buffer (2.5M NaCl, 100mM EDTA, 10mM Tris and 1% N-lauroylsarcosine pH9.5, with *ex tempore* addition of 1% Triton X-100 and 1% DMSO) for 2h at 4°C. Slides were placed in an electrophoresis tank, incubated with fresh TBE for 30min to allow DNA to unwind, and subjected to electrophoresis for 32min at 72V at RT. Slides were rinsed, stained and stored as above. Acquisition and analysis of 100 comets per condition were performed at 100× magnification using an epifluorescence microscope (Ni-E, Nikon) and Komet v.5.5 software (Andor). DNA damage was measured by quantifying tail DNA as % total DNA.

**In vivo study.** Experiments were performed under UK Home Office approved project licence (PPL 30/3395. SK-CO-1 cells (10<sup>7</sup>/mouse in 50% Matrigel, BD Bioscience) were injected into the subcutaneous tissues of the back of 6 week-old female CD-1 nude mice (Envigo). When tumors reached 100 mm<sup>3</sup>, mice were randomly divided into two groups (n=10) for treatment with control (PBS) or 100 mg/kg xentuzumab twice weekly by intraperitoneal injection. Body weights and tumor volumes were measured 5 times a week for 3 weeks. On the final day, mice were injected intraperitoneally with BrdU, and after 2h mice were humanely culled and tissues processed for IHC.

**Immunohistochemistry.** Murine tissues were used under PPL 30/3395 and PIL I9BC08CD7. Freshly cut 6 µm sections of formalin-fixed paraffin embedded tumor and overlying mouse skin were stained using EnVision G2 Double stain System (Agilent Technologies) according to manufacturers' instructions, with additional blocking using 3% H<sub>2</sub>O<sub>2</sub> for 20min and mouse-on-mouse blocking for mouse antibodies (MKB-2213, Vector Laboratories), and with primary antibodies listed in Supplementary Table S1.

**Statistics.** GraphPad Prism v7 was used to perform Student's t-test to compare means of 2 groups, and one-way ANOVA with Tukey post-test to compare >2 groups. All tests were 2-sided and p<0.05 (\*), p<0.01 (\*\*) and p<0.001 (\*\*\*) were considered significant.

### Supplementary references

1. Bohula EA, Salisbury AJ, Sohail M, Playford MP, Riedemann J, Southern EM, et al. The efficacy of small interfering RNAs targeted to the type 1 insulin-like growth factor receptor (IGF1R) is influenced by secondary structure in the IGF1R transcript. *J Biol Chem.* 2003;278(18):15991-7.
2. Aleksic T, Gray NE, Wu X, Rieunier G, Osher E, Mills J, et al. Nuclear IGF-1R interacts with regulatory regions of chromatin to promote RNA polymerase II recruitment and gene expression associated with advanced tumor stage. *Cancer Res.* 2018.
3. Chou TC. Drug combination studies and their synergy quantification using the Chou-Talalay method. *Cancer Res.* 2010;70(2):440-6.
4. Ramboer E, De Craene B, De Kock J, Berx G, Rogiers V, Vanhaecke T, et al. Development and characterization of a new human hepatic cell line. *EXCLI J.* 2015;14:875-89.
5. Meneret A, Ahmar-Beaugendre Y, Rieunier G, Mahlaoui N, Gaymard B, Apartis E, et al. The pleiotropic movement disorders phenotype of adult ataxia-telangiectasia. *Neurology.* 2014;83(12):1087-95.
6. Manders EM, Stap J, Brakenhoff GJ, van Driel R, and Aten JA. Dynamics of three-dimensional replication patterns during the S-phase, analysed by double labelling of DNA and confocal microscopy. *J Cell Sci.* 1992;103 ( Pt 3):857-62.
7. Schwab RA, and Niedzwiedz W. Visualization of DNA replication in the vertebrate model system DT40 using the DNA fiber technique. *J Vis Exp.* 2011(56):e3255.
8. Chitnis MM, Lodhia KA, Aleksic T, Gao S, Protheroe AS, and Macaulay VM. IGF-1R inhibition enhances radiosensitivity and delays double-strand break repair by both non-homologous end-joining and homologous recombination. *Oncogene.* 2014;33(45):5262-73.
9. Lodhia KA, Gao S, Aleksic T, Esashi F, and Macaulay VM. Suppression of homologous recombination sensitizes human tumor cells to IGF-1R inhibition. *Int J Cancer.* 2015;136(12):2961-6.
10. Kotsantis P, Silva LM, Irmischer S, Jones RM, Folkes L, Gromak N, et al. Increased global transcription activity as a mechanism of replication stress in cancer. *Nat Commun.* 2016;7:13087.
11. Collins AR, Oscoz AA, Brunborg G, Gaivao I, Giovannelli L, Kruszewski M, et al. The comet assay: topical issues. *Mutagenesis.* 2008;23(3):143-51.
12. Poletto M, Yang D, Fletcher SC, Vendrell I, Fischer R, Legrand AJ, et al. Modulation of proteostasis counteracts oxidative stress and affects DNA base excision repair capacity in ATM-deficient cells. *Nucleic Acids Res.* 2017;45(17):10042-55.



Western blotting and immunofluorescence				
Primary antibodies	Supplier	Species	Dilution	Catalogue number
P-IGF-1R Tyr1135/1136	Cell Signaling Technology	Rabbit	1/1000	#3024
IGF-1R $\beta$	Cell Signaling Technology	Rabbit	1/1000	#3027
P-AKT Ser473	Cell Signaling Technology	Rabbit	1/1000	#4060
AKT	Cell Signaling Technology	Rabbit	1/1000	#9272
P-CHK1 Ser345	Cell Signaling Technology	Rabbit	1/1000	#2348
CHK1	Santa Cruz	Mouse	1/1000	sc-8408
RRM1	Santa Cruz	Goat	1/1000	sc-11733
RRM2	Santa Cruz	Rabbit	1/1000	sc-10844
P-ERK Thr202/Tyr204	Cell Signaling Technology	Rabbit	1/1000	#9101
ERK	Cell Signaling Technology	Mouse	1/1000	#4696
P-RPA Ser33	Bethyl Laboratories	Rabbit	1/1000	A300-246A
RPA	Cell Signaling Technology	Goat	1/1000	#2208
P-S6 Ser235/236	Cell Signaling Technology	Rabbit	1/1000	#2211
S6	Cell Signaling Technology	Rabbit	1/1000	#2217
P-KAP1 Ser824	Bethyl Laboratories	Rabbit	1/1000	A300-767A
KAP1	Bethyl Laboratories	Rabbit	1/1000	A300-275A
$\beta$ -actin	Sigma	Mouse	1/5000	A2228
$\beta$ -tubulin	Sigma	Mouse	1/5000	T4026
gH2AX	Millipore	Mouse	1/500	05-636
53BP1	Novus Biologicals	Rabbit	1/500	NB-100-304
Cyclin A	Santa Cruz	Mouse	1/100	sc-271682
p53R2	Abcam	Rabbit	1/1000	ab8105
P-Ser1981 ATM	Cell Signaling Technology	Mouse	1/1000	#4526
IdU	BD Bioscience	Mouse	1/100	347580
CIdU	Abcam	Rat	1/500	ab6326
Secondary antibodies	Supplier	Species	Dilution	Catalogue number
IRDye 680CW anti-mouse	LI-COR	Mouse	1/15000	926-32212
IRDye 800CW anti-rabbit	LI-COR	Rabbit	1/10000	926-32213
AlexaFluor 488	ThermoFisher	Mouse	1/2000	A-11001
AlexaFluor 594	ThermoFisher	Rabbit	1/2000	R37117
AlexaFluor 594	ThermoFisher	Rat	1/300	A-11007
Immunohistochemistry				
Primary antibodies	Supplier	Species	Dilution	Catalogue number
P-AKT Ser473	Cell Signaling Technology	Rabbit	1/100	#4060
Cleaved Caspase 3	Cell Signaling Technology	Rabbit	1/150	#9661
RRM2	Santa Cruz	Goat	1/400	sc-10846
BrdU	BD Bioscience	Mouse	1/50	347580
ATM	Abcam	Rabbit	1/300	ab3280

**Supplementary Table S1.** Antibodies used in western blotting, immunofluorescence and IHC.

**A. 0.1  $\mu$ M**

Rank	Target	Compound
1	AKT	MK-2206
2	EGFR	Lapatinib Ditosylate
3	CDK4/6	Abemaciclib (LY2835219)
4	HADC	CUDC-101
5	EGFR	BMS-599626
6	MEK	PD318088
7	Topoisomerase I	Irinotecan
8	ATM	KU-55933
9	Estrogen receptor	Fulvestrant
10	MDM2	Nutlin 3
11	PI3K, DNA-PK	PIK-75
12	DNA/RNA synthesis	Flucytosine

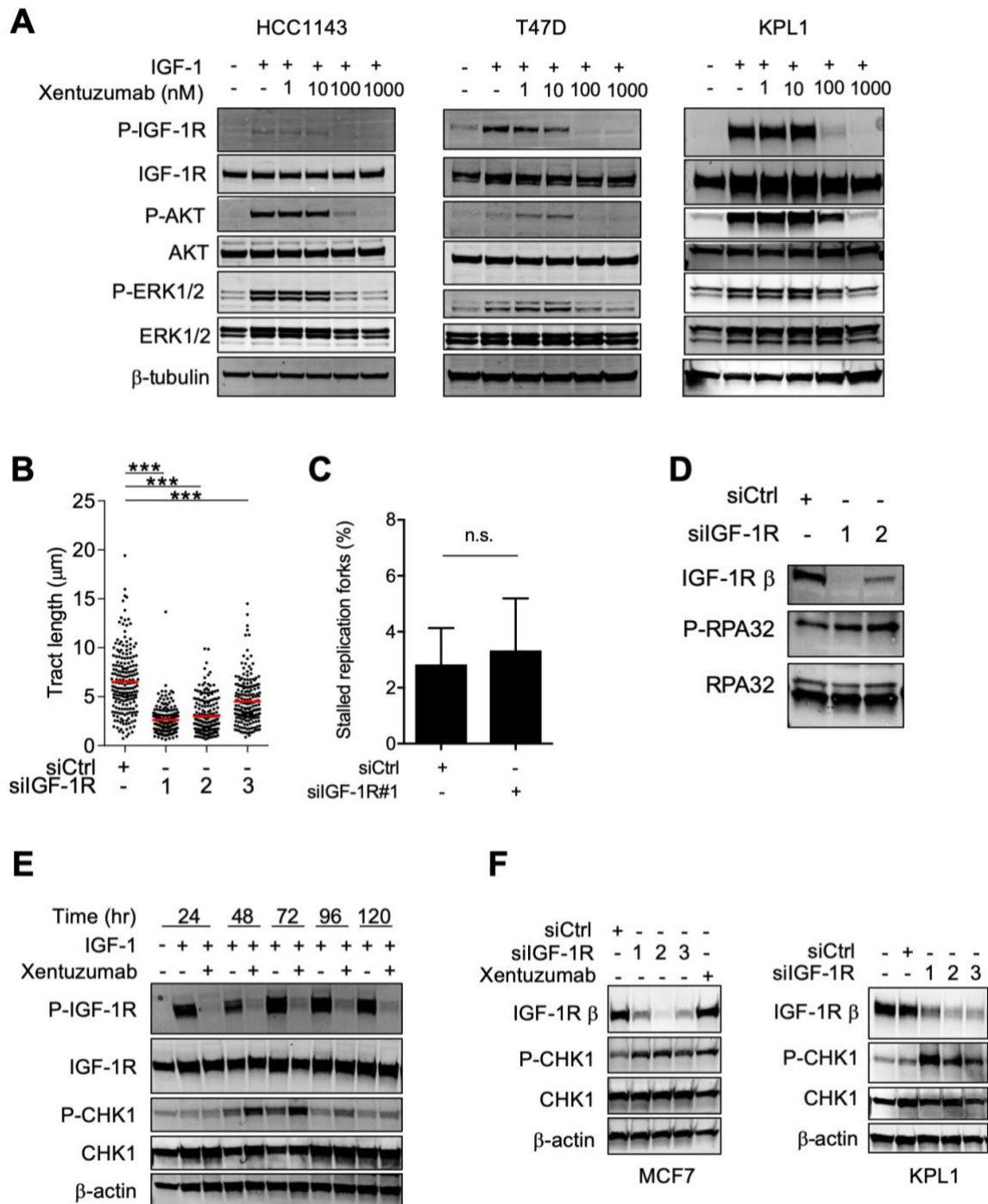
**B. 1  $\mu$ M**

Rank	Target	Compound
1	EGFR	Lapatinib Ditosylate
2	EGFR	CUDC-101
3	CDK1	Ro-3306
4	EGFR	BMS-599626
5	RAD51	BO2
6	MEK	PD318088
7	ATM	KU-55933
8	Mdm2/p53	Nutlin 3
9	Estrogen receptor	Fulvestrant
10	Aurora kinase	Tozasertib (VX-680)
11	ATM	KU-60019
12	CDK	PD0332991

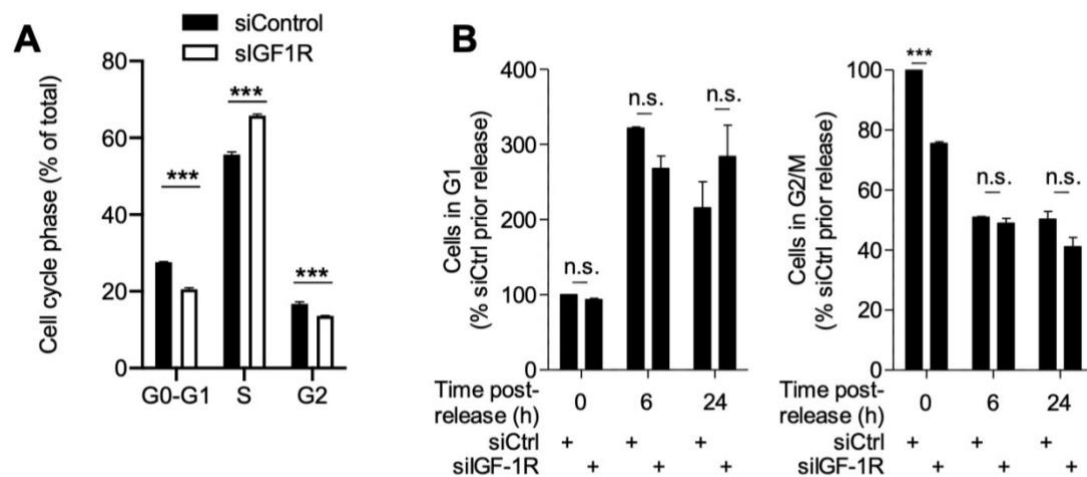
**C. 10  $\mu$ M**

Rank	Target	Drug name
1	ATM	KU-55933
2	MEK	PD318088
3	EGFR	Lapatinib Ditosylate
4	EGFR	BMS-599626
5	Estrogen receptor	Fulvestrant
6	MRE11	Mirin
7	MEK	BIX 02189
8	PARP	ABT-888
9	DNA/RNA synthesis	Flucytosine (Ancobon)
10	mTOR	Deforolimus (MK-8669)
11	WRN	NSC 19630
12	Aurora kinase	Hesperadin

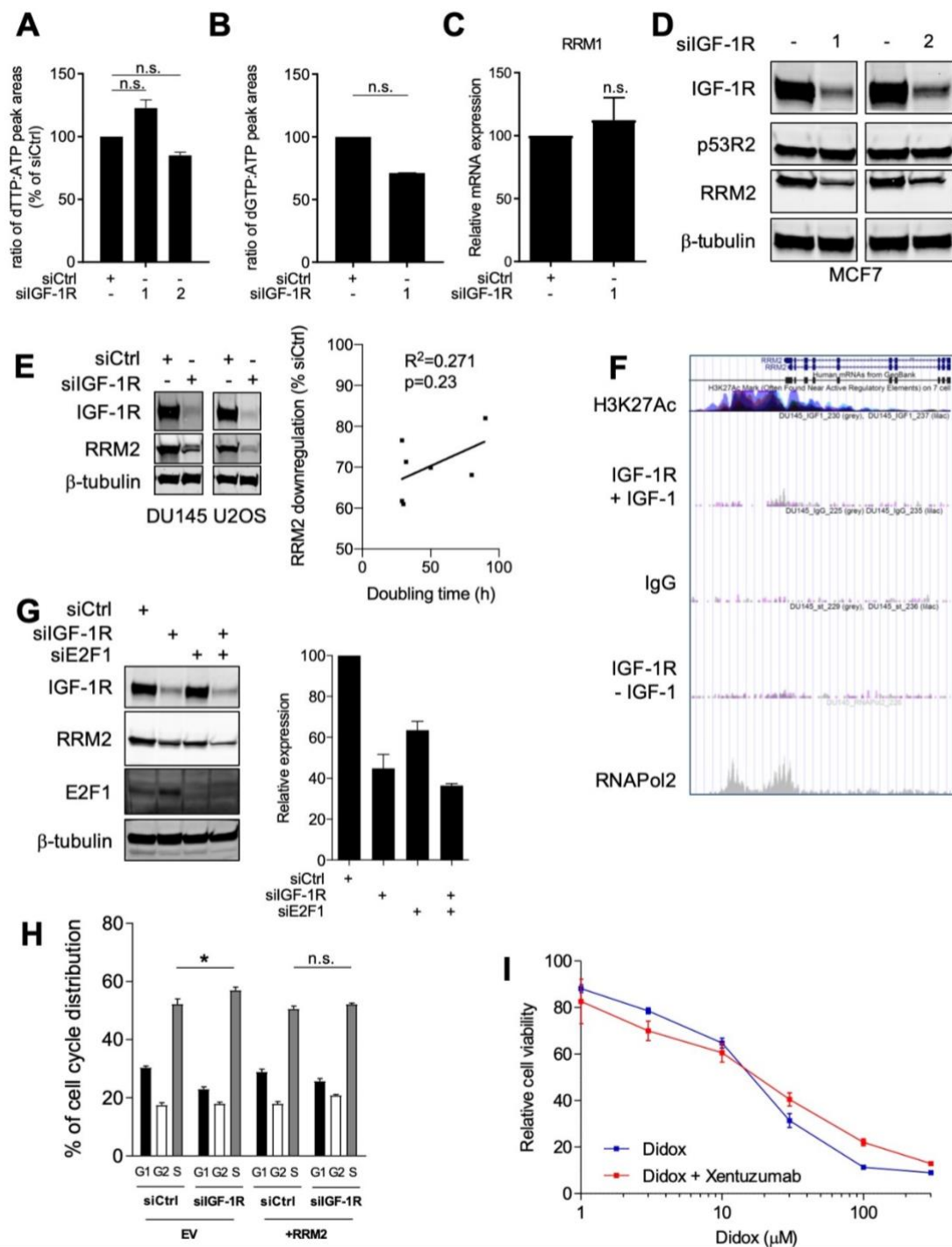
**Supplementary Table S2. Compound screen in MCF7 cells with xentuzumab.** Tables show top ranked screen hits in cells treated with 1  $\mu$ M xentuzumab plus compounds at 0.1, 1.0 or 10  $\mu$ M.



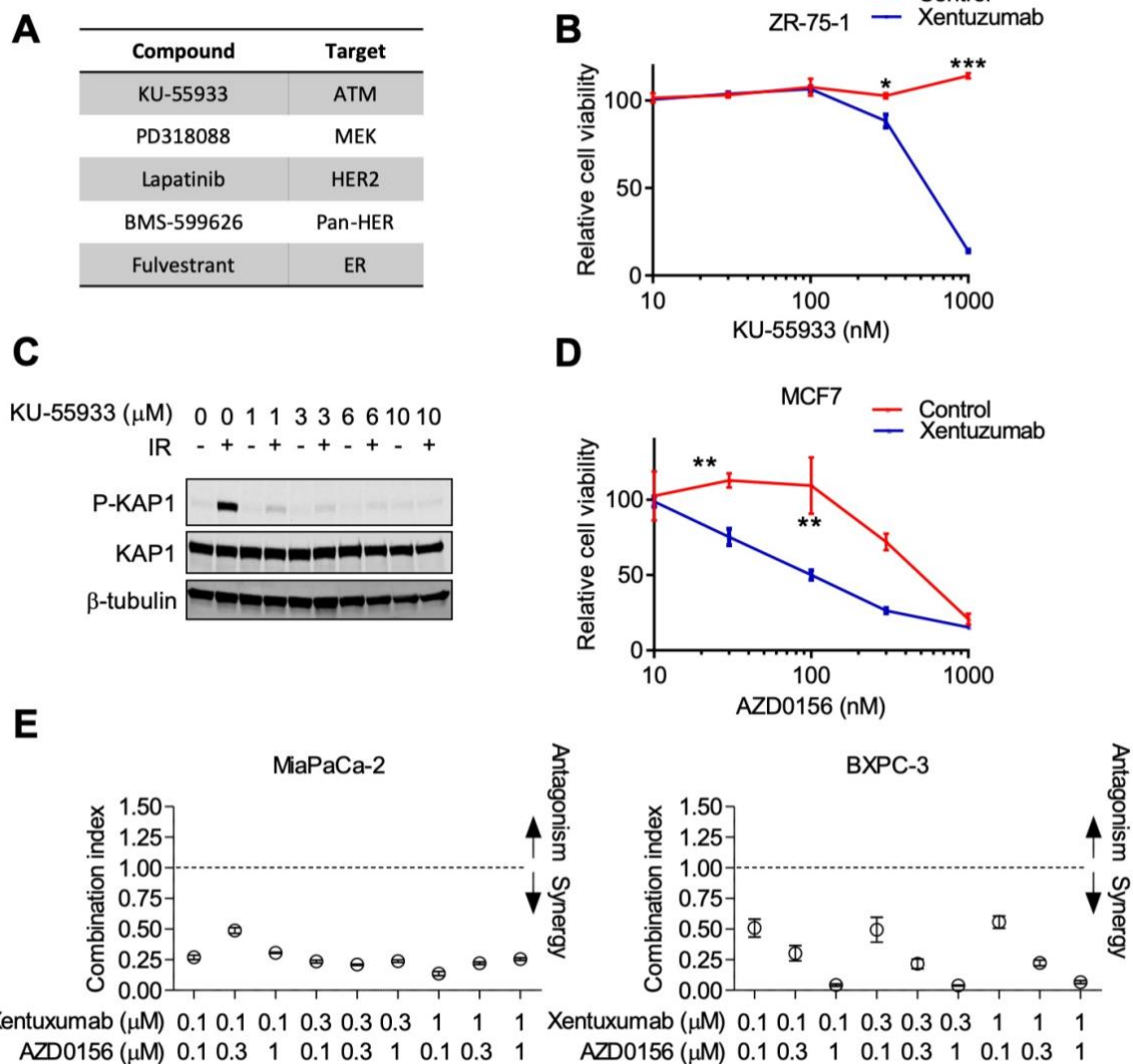
**Supplementary Figure S1. IGF-1R targeting slows replication fork progression and activates ATR-dependent CHK1 phosphorylation.** **A.** Serum starved cells were treated with xentuzumab for 5 days and in the final 15 min with 50nM IGF-1. **B.** KPL1 cells transfected with Control (siCtrl) or 3 independent IGF-1R siRNAs were processed 72h later for DNA fiber analysis and replication tract length (CldU/IdU) was quantified. Red line: median. **C.** MCF7 cells were siRNA-transfected and analysed by DNA fiber assay as Figure 1E-F, and stalled forks were quantified (n=200 tracts per condition). There was a low percentage of stalled forks, with no difference between siControl and siIGF-1R transfectants. **D.** MCF7 cells were siRNA transfected and analysed after 72h for RPA32 phosphorylation. **E.** Serum starved MCF7 cells were treated with xentuzumab for 1-5 days and in the final 15 min with 50nM IGF-1. CHK1 Ser345 phosphorylation was increased in xentuzumab-treated cells, peaking at 72h. **F.** MCF7 and KPL1 cells were transfected with Control (siCtrl) or 3 independent IGF-1R siRNAs and lysed 72h later or treated with 100nM xentuzumab for 72h and lysed for western blot.



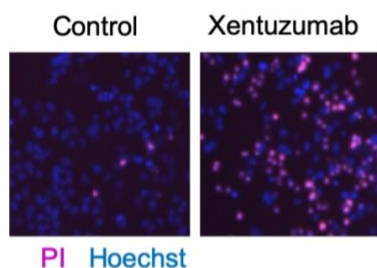
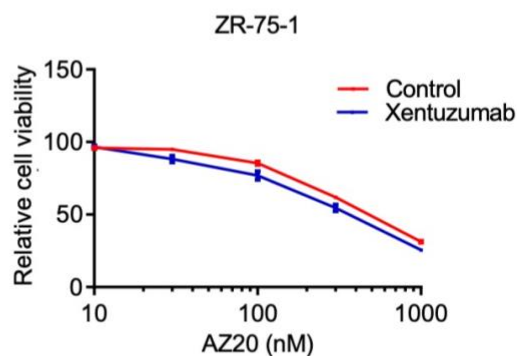
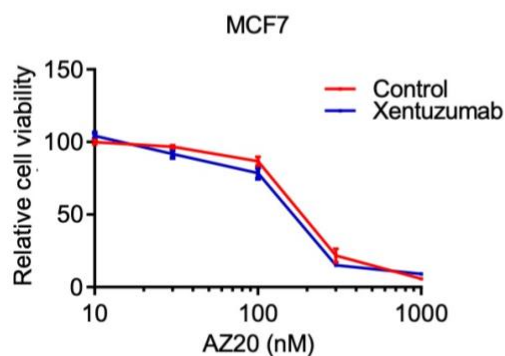
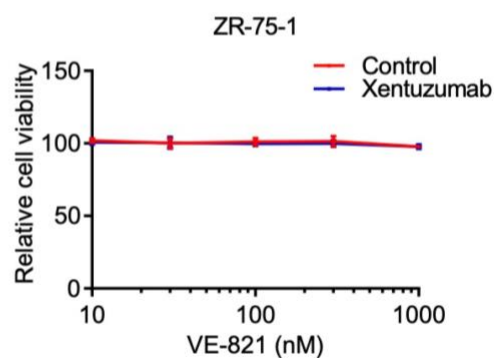
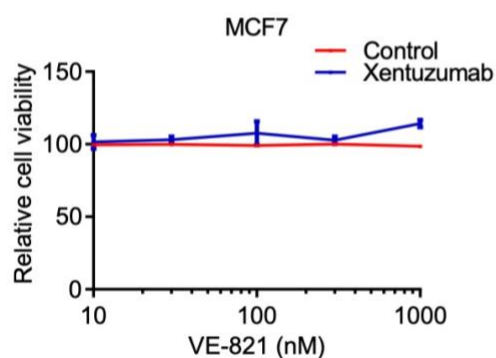
**Supplementary Figure S2. IGF-1R depletion causes accumulation of cells in S phase.** **A.** MCF7 cells were siRNA-transfected and collected after 48h for cell cycle analysis (n=3 independent experiments). **B.** MCF7 cells siRNA transfected and nocodazole treated as in Figure 2C-D were harvested after 42-68h for cell cycle analysis (n=3 independent experiments). Graphs: left: cells in G1; right, cells in G2/M.



**Supplementary Figure S3. IGF-1R regulates RRM2 levels and RNR activity.** **A, B.** MCF7 cells were transfected with Control (siCtrl) or IGF-1R siRNAs and after 48h processed for dTTP (A) and dGTP (B) analysis, showing mean  $\pm$  SEM fold change as % siCtrl. **C.** *RRM1* mRNA quantified in MCF7 cells after siRNA-transfection as A-B (mean  $\pm$  SEM, 3 independent analyses). **D.** MCF7 cells were transfected with Control (siCtrl) or siIGF1R\_1 and analysed after 72hr by western blot. **E.** Cells were transfected with siControl (siCtrl) or siIGF-1R\_1 and lysed after 48h. Graph to right: doubling time of 5 breast cancer cell lines (as Figure 3G), DU145 and U2OS plotted against % RRM2 downregulation induced by IGF-1R depletion (% siControl) showing lack of correlation. **F.** UCSC browser image: IGF-1R ChIP-seq in DU145 cells treated  $\pm$  IGF-1 [2]. RRM2 promoter is enriched for RNAPol2 recruitment and H3K27 acetylation, often found near active regulatory elements (public data, ENCODE), but not IGF-1R (duplicate samples, grey/lilac, or IgG, control ChIP). **F.** MCF7 were siRNA transfected and harvested after 48h for western blot. Graph: quantification of duplicate independent blots showing mean  $\pm$  range RRM2 protein, reduced by siIGF-1R\_1 to 45 $\pm$ 10%, siE2F1 to 63 $\pm$ 6%, co-depletion 36 $\pm$ 2%. **G.** Stably transfected MCF7 cells transfected with siCtrl or siIGF1R\_1 and 48hr later processed for cell cycle analysis.

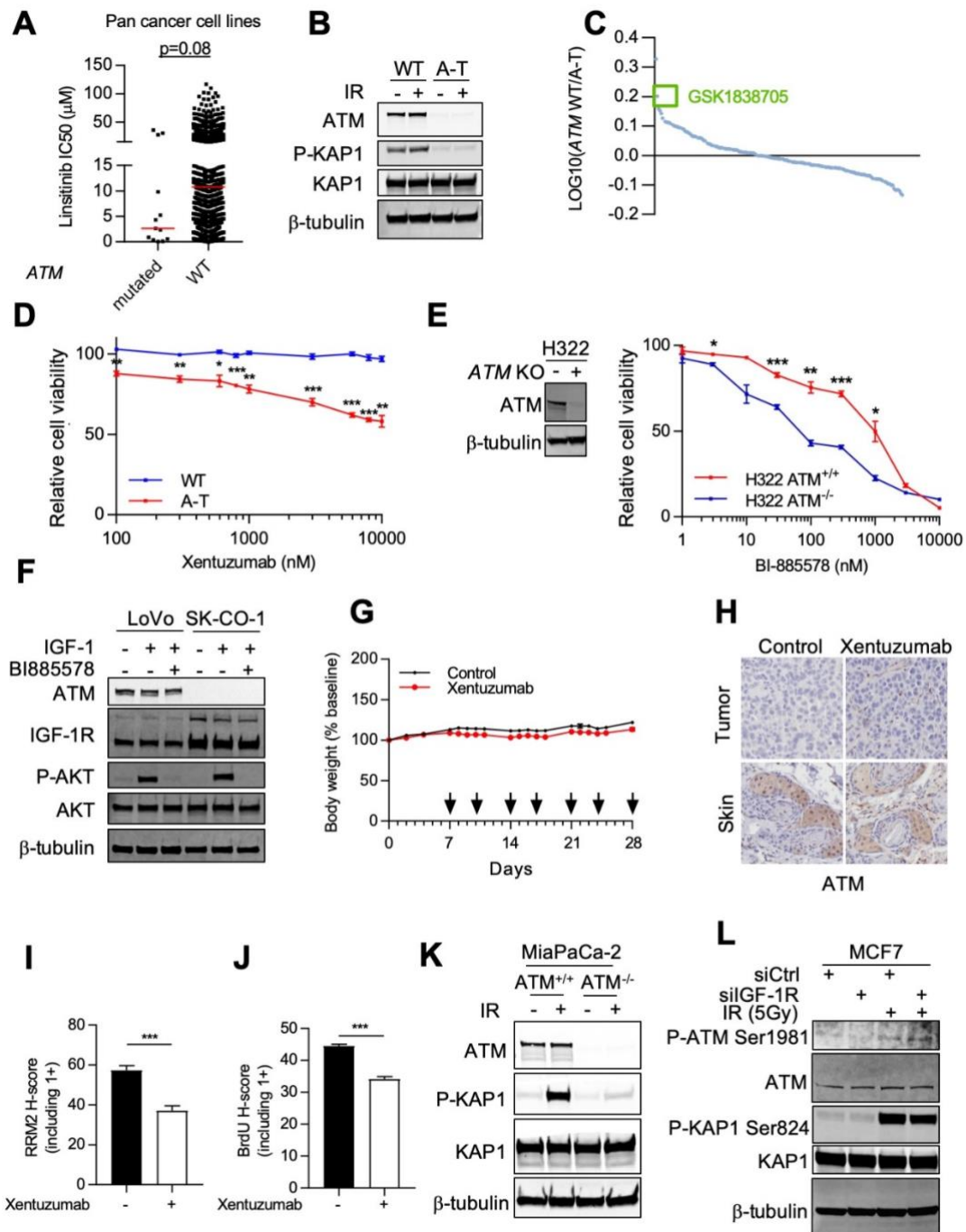


**Supplementary Figure S4. Testing xentuzumab with ATM or ATR inhibitors.** **A.** Top 5 screen hits identified in common at compound screening concentrations of 0.1, 1 and 10 μM in MCF7 cells. **B.** ZR-75-1 cells were treated with KU-55933 alone or with 1 μM xentuzumab, and viability was measured after 5 days. Xentuzumab induced significant reduction in cell viability. **C.** MCF7 cells were pre-treated with 1-10 μM KU-55933 for 48h, irradiated (5Gy) and collected after 30min for western blot. **D.** MCF7 cells were treated with AZD0156 alone or with 1 μM xentuzumab, and viability was measured after 5 days. **E.** Combination indices (CI) calculated from viability data on MiaPaCa-2 and BXPC-3. CI values <0.8 indicate synergy and <0.3, strong synergy.

**A****B****C**

**Supplementary Figure S5. Testing xentuzumab with inhibitors of ATM and ATR.** **A.** Image of representative PI/Hoechst-stained wells imaged on Celigo cytometer, as shown in Figure 5F. **B, C.** MCF7 (left) and ZR-75-1 (right) cells treated with ATR inhibitors AZ20 (B) or VE-821 (C) alone or with 1  $\mu$ M xentuzumab, and viability measured after 5 days.





**Supplementary Figure S6. Importance of IGF-1R in ATM null cells.** **A.** Pan-cancer analysis in 926 cell lines testing association of ATM homozygous mutations with sensitivity to IGF-1R inhibitor linsitinib (cancerrxgene.org). **B.** ATM WT and A-T fibroblasts were irradiated (5Gy) and collected after 30 min for western blot. **C.** ATM WT and A-T fibroblasts treated with 0.1μM kinase inhibitors (188compounds), viability measured after 3 days. Graph: compounds ranked by ratio  $\log_{10}$  viability ATM<sup>WT</sup>/A-T fibroblasts, highlighting IGF-1R inhibitor GSK1838705. **D.** ATM WT and A-T fibroblasts treated with xentuzumab, viability measured after 5 days. **E.** Isogenic H322 ATM proficient/deficient cells treated with BI-885578, viability assayed as D. Blot confirms ATM status. **F.** Serum-starved CRC cells were pre-treated with BI-885578 for 24h and in the final 15 min with 50 nM IGF-1. **G.** Body weight of tumor-bearing mice treated twice weekly (arrows) as Figure 6F. **H.** IHC staining for ATM after treatment with control or xentuzumab for 3 weeks showing ATM-negative SK-CO-1 tumor, ATM-positive mouse skin. **I-J.** Quantification of immunohistochemical signal for RRM2 (I) and BrdU (J) from figure 6G, including weak positive (1+) cells. **L.** MCF7 cells were siRNA-transfected and after 48h irradiated and collected after 30min for western blot.